

# 1 Geothermal Modeling in Complex Geological Systems with 2 ComPASS

3 A. Armandine Les Landes\*, L. Beaude<sup>†</sup>, D. Castanon Quiroz<sup>‡§</sup>, L. Jeannin,<sup>¶</sup>  
S. Lopez<sup>¶</sup>, R. Masson<sup>\*\*</sup>

4 January 2023

5 **Keywords:** geothermal reservoir modeling, multi-component multi-phase flow, unstructured  
6 meshes, faulted and fractured reservoir, deviated wells

## 7 Abstract

8 Faults and fractures in deep geothermal reservoirs not only control fluid flow and heat  
9 transfer, but also provide feed zones for production wells. Modeling operation of geothermal  
10 fields actually requires explicitly taking into account objects with different spatial scales such  
11 as the reservoir itself, faults and fractures and also the injection and production wells.

12 Our main objective in developing the ComPASS geothermal flow simulator, was to take into  
13 account all of these geometric constraints in a flow and heat transfer numerical model using  
14 generic unstructured meshes. In its current state, the code provides a parallel implementation  
15 of a spatio-temporal discretization of the non-linear equations driving compositional multi-  
16 phase thermal flows in porous fractured media on unstructured meshes. It allows an explicit  
17 discretization of faults and fractures as 2D hybrid objects, immersed in a 3D matrix. Similarly,  
18 wells are modeled as one dimensional graphs discretized by edges of the 3D mesh which allows  
19 arbitrary multi-branch wells. The resulting approach is particularly flexible and robust in terms  
20 of modeling.

21 Its practical interest is demonstrated by different case studies: we successively focus on the  
22 production of a deep geothermal reservoir in a typical EGS (Engineered Geothermal System)  
23 context, on the doublet exploitation of a faulted high-enthalpy liquid-dominated reservoir, on the  
24 production from a vapor-dominated reservoir, and on the modeling of a large-scale geothermal  
25 system by taking into account the soil-atmosphere interaction and recharge effects.

## 26 1 Introduction

27 Exploitation of deep geothermal reservoirs allows clean, non-intermittent heat and/or power  
28 production with very limited environmental impact and may have a substantial contribution to the

\*BRGM, 3 avenue Claude-Guillemen, BP 36009, 45060 Orléans Cedex 2, France, A.ArmandineLesLandes@brgm.fr

<sup>†</sup>BRGM, 3 avenue Claude-Guillemen, BP 36009, 45060 Orléans Cedex 2, France, l.beaude@brgm.fr

<sup>‡</sup>Université Côte d'Azur, Inria, CNRS, LJAD, UMR 7351 CNRS, team Coffee, Parc Valrose 06108 Nice Cedex 02, France.

<sup>§</sup>Instituto de Investigaciones en Matemáticas Aplicadas y en Sistemas, Universidad Nacional Autónoma de México, Circuito Escolar s/n, Ciudad Universitaria C.P. 04510 Cd. Mx. (México), daniel.castanon@iimas.unam.mx

<sup>¶</sup>STORENGY, 12 rue Raoul Nordling - Djinn - CS 70001 92274 Bois Colombes Cedex, France, laurent.jeannin@storengy.com

<sup>||</sup>BRGM, 3 avenue Claude-Guillemen, BP 36009, 45060 Orléans Cedex 2, France, s.lopez@brgm.fr

<sup>\*\*</sup>Université Côte d'Azur, Inria, CNRS, LJAD, UMR 7351 CNRS, team Coffee, Parc Valrose 06108 Nice Cedex 02, France, roland.masson@univ-cotedazur.fr

29 decarbonization of our economy [24]. At all stages of exploration and development of geothermal  
30 projects, numerical modeling of subsurface flows has become an essential tool. Flow modeling is used  
31 on one hand in the exploration phases to assess the geothermal potential, to validate conceptual  
32 hypothesis and on the other hand in the development of geothermal assets to predict production flow  
33 rates (*e.g.* among others [25], [35], [18], [26]). Not only do the models provide a coherent vision of  
34 the geothermal system by integrating all the data and measurements, but above all they represent a  
35 quantitative tool for anticipating production and development.

36 Faults and fractures exert a dominant control on subsurface fluid flows and transfers in geothermal  
37 reservoirs. For example, in tectonically active areas such as high temperature magmatic settings,  
38 fault zones act often as permeable corridors. Concerning enhanced Geothermal Systems (EGS),  
39 where hydraulic stimulation ensures connection with a fault network, flow takes place mostly in  
40 a fracture network. Role of discontinuities has also been acknowledged as a major control in the  
41 thermal structure of sedimentary basins where they can act as connections between aquifer levels  
42 [30, 34, 40]. Finally, most of the time, feed zones of geothermal wells are found at the intersection of  
43 the well path and fault zones or fractures [23]. The flow is thus mainly dominated by the connectivity  
44 and conductivity of the fracture/fault network in interaction with the surrounding matrix medium.

45 Physical modeling of flow and heat exchange is based on molar and energy conservation equations  
46 expressed locally, accounting for multi-phase compositional thermal Darcy flow model and thermo-  
47 dynamic equilibrium. In terms of spatial discretization, most numerical models are based on the use  
48 of structured grids - rectangular cartesian grids or Corner Point grids [27] - which overly simplify  
49 geology and fail to reproduce the geometrical complexity of the geological bodies, fault and fracture  
50 networks and deviated wells. An accurate modeling of the geothermal fields requires explicitly tak-  
51 ing into account all these objects and their different characteristic sizes. This realization was the  
52 main motivation for putting generic unstructured meshes and complex geometries at the heart of the  
53 development of the ComPASS geothermal flow simulator with the ambition to improve the accuracy  
54 and the representativeness of numerical models and simulation workflows and facilitate the back and  
55 forth between geology and flow modeling.

56 This paper presents the ComPASS code with a special focus on recent developments and how  
57 the versatility of unstructured meshes to model faults, fractures and deviated wells with adapted  
58 numerical schemes may be exploited. Indeed, such meshes can be used to exactly match any geological  
59 structure and two dimensional geometrical objects and boundaries (geological interfaces, faults . . . )  
60 or one dimensional sharp features (surfaces intersection, well paths . . . ).

61 In terms of physics, the flow model is formulated using a classic multi-phase multi-component  
62 Coats-type approach [16]. Spatial discretization relies on the Vertex Approximate Gradient (VAG)  
63 scheme [21, 12, 13]. This finite volume scheme is valid on generic polyhedral conforming meshes and  
64 has essentially nodal unknowns (cell unknowns can be eliminated to improve computing time). This  
65 makes it particularly adapted to conforming unstructured tetrahedral meshes.

66 Thanks to the use of unstructured meshes, fractures and faults are accurately described as two di-  
67 mensional (polygonal) surfaces embedded in the rock matrix. Physical model of conductive fractures  
68 is obtained from a three-dimensional physical model by integration and averaging along the width  
69 of each discontinuity. The Darcy flow in the matrix medium is then coupled with two dimensional  
70 flow in the fractures and faults using transmission conditions at the matrix-fracture interface, the  
71 VAG scheme being extended with fracture faces unknowns to handle this family of hybrid models  
72 including faults and fractures [12, 13, 42]. An important point is that, compared to other control  
73 volume schemes, this extended version of the VAG scheme avoids the mixing of the control volumes  
74 at the matrix fracture interfaces, which is of great benefit for its coupling with a transport model  
75 [42]. Concerning wells, they are discretized as a subset of edges of the mesh. This approach provides  
76 an efficient way to represent slanted and multi-branch wells. The fluxes connecting the well with  
77 the 3D matrix and the 2D fracture network at each node of the well is computed using Peaceman's

78 approach [32, 33].

79 Moreover, special attention has also been paid to the numerical performance: the code is massively  
80 parallel and good scalability properties have been obtained to take advantage of the multi-core and  
81 parallel architectures of current computers and supercomputers [42]. Another main focus concerns  
82 the development of specific boundary conditions describing recharges or shallow processes in the  
83 vadose zone [10, 7] providing a description of the exchanges of the geothermal reservoir with its  
84 environment.

85 The remainder of the paper is organized as follows. The first part presents the physical model of  
86 multi-phase compositional geothermal flows in fractured and faulted geothermal reservoirs and the  
87 specific numerical discretizations in the ComPASS code. In addition, the approaches used in terms  
88 of meshing, parallelization and numerical performances are detailed. The second part is devoted  
89 to different numerical tests, which illustrate the advantages of the developed approach. The first  
90 three cases were built from development studies on geothermal fields and concern respectively the  
91 operation of an EGS-like faulted and fractured reservoir exploited by a geothermal doublet, a liquid  
92 dominated high-enthalpy reservoir crossed by major faults and a high enthalpy low pressure steam  
93 reservoir. The last case study use a two-component air-water model describing a natural geothermal  
94 system, accounting for soil-atmosphere interaction and recharge.

## 95 2 Model description

96 In this section, we detail the compositional multi-phase model currently implemented in the Com-  
97 PASS code as well as the way in which the faults and wells are represented and the numerical scheme  
98 associated with the unstructured meshes. Numerical and implementation aspects are then discussed.

### 99 2.1 Multi-phase multi-component model in fractured media

100 The physical model is based on a Coats' type formulation [16] also known as a natural vari-  
101 ables formulation. It extends the work by Eymard *et al.* [22] and Brenner *et al.* [13] to non-  
102 isothermal flows including fractures. We refer the interested reader to the detail version by Xing *et*  
103 *al.* [42]. Additional information is also available in the code documentation which is available at  
104 <https://charms.gitlabpages.inria.fr/ComPASS>.

105 The physical system is described by an arbitrary set of components  $\mathcal{C}$  and an arbitrary set  
106 of phases  $\mathcal{P}$ . Each phase  $\alpha \in \mathcal{P}$  is described by its non-empty subset of possible components  
107  $\mathcal{C}^\alpha \subset \mathcal{C}$ . Respectively, we denote  $\mathcal{P}_i$  the non-empty subset of possible phases of the component  
108  $i \in \mathcal{C}$  such that  $\mathcal{P}_i = \{\alpha \in \mathcal{P}; i \in \mathcal{C}^\alpha\}$ . Finally, several so-called contexts are introduced to describe  
109 different physical states. They are defined by the set of present phases and are noted  $Q \subset \mathcal{P}$ . This  
110 framework is very generic and can be used to describe very complex fluids. On a very simple example,  
111 a classical sub-critical pure water system would be described by  $\mathcal{C} = \{\text{water}\}$ ,  $\mathcal{P} = \{\text{liquid}, \text{gas}\}$ ,  
112 and  $Q \in \{\{\text{liquid}\}, \{\text{gas}\}, \{\text{liquid}, \text{gas}\}\}$  with the first two contexts corresponding to monophasic  
113 states and the later to a diphasic state.

114 For a given set of present phases  $Q$ , it may occur that a component  $i \in \mathcal{C}$  does not belong to the  
115 subset  $\cup_{\alpha \in Q} \mathcal{C}^\alpha \subset \mathcal{C}$ . Hence, we define  $\bar{\mathcal{C}}_Q$  the subset of absent components, that are absent in any  
116 of the present phases defined by  $Q$ .

117 Thermodynamic properties of each phase  $\alpha \in \mathcal{P}$  depend on the phase pressure  $P^\alpha$ , the temper-  
118 ature  $T$  and the phase molar fractions  $C^\alpha = (C_i^\alpha)_{i \in \mathcal{C}^\alpha}$ .  $S^\alpha$  denotes the saturation,  $n_i$  the number of  
119 moles of the component  $i \in \mathcal{C}$  per unit pore volume.

120 Altogether, the formulation uses the following set of unknowns (see [42] for more details):

$$X = ((P^\alpha)_{\alpha \in Q}, T, (S^\alpha)_{\alpha \in Q}, (C^\alpha)_{\alpha \in Q}, (n_i)_{i \in \bar{\mathcal{C}}_Q}, Q). \quad (1)$$

For each context  $Q$ , the number of moles of the present component  $i \in \mathcal{C} \setminus \overline{\mathcal{C}_Q}$  per unit pore volume, is defined by:

$$n_i = \sum_{\alpha \in Q \cap \mathcal{P}_i} \xi^\alpha(P^\alpha, T, C^\alpha) S^\alpha C_i^\alpha$$

where  $\xi^\alpha$  is the phase molar density. Note that the conditional unknowns  $(n_i)_{i \in \overline{\mathcal{C}_Q}}$  are used to avoid the singularity of the Jacobian matrix and to track the appearance of the phase(s) containing component  $i \in \overline{\mathcal{C}_Q}$ . The molar conservation for each component and energy conservation take the following form:

$$\begin{cases} \phi \partial_t n_i + \nabla \cdot \mathbf{q}_i = 0, & i \in \mathcal{C}, \\ \phi \partial_t E + (1 - \phi) \partial_t E_r + \nabla \cdot \mathbf{q}_e = 0 \end{cases} \quad (2)$$

where  $\phi$  is the rock porosity assumed constant in time,  $E$  and  $E_r$  are respectively the fluid internal energy and rock energy per unit rock volume.  $\mathbf{q}_i$  denotes the molar flux of component  $i$ . It is obtained from the generalized Darcy law for each phase:

$$\mathbf{q}_i = \sum_{\alpha \in Q \cap \mathcal{P}_i} C_i^\alpha \xi^\alpha(P^\alpha, T, C^\alpha) \mathbf{V}^\alpha$$

with

$$\mathbf{V}^\alpha = -\mathbf{K} \frac{k_r^\alpha(S^\alpha)}{\mu^\alpha(P^\alpha, T, C^\alpha)} (\nabla P^\alpha - \rho^\alpha(P^\alpha, T, C^\alpha) \mathbf{g})$$

where  $\mathbf{K}$  is the rock permeability tensor,  $k_r^\alpha$  is the relative permeability of the phase  $\alpha$ ,  $\mu^\alpha$  its viscosity and  $\rho^\alpha$  its mass density.

For each context  $Q$ , the fluid internal energy writes:

$$E = \sum_{\alpha \in Q} \xi^\alpha(P^\alpha, T, C^\alpha) S^\alpha e^\alpha(P^\alpha, T, C^\alpha)$$

where  $e^\alpha$  is the molar internal energy of the phase  $\alpha$ .

The total energy flux  $\mathbf{q}_e$  is defined by:

$$\mathbf{q}_e = \sum_{\alpha \in Q} h^\alpha(P^\alpha, T, C^\alpha) \xi^\alpha(P^\alpha, T, C^\alpha) \mathbf{V}^\alpha - \lambda \nabla T$$

where  $\lambda$  is the equivalent conductivity of the rock/fluid mixture and  $h^\alpha$  the molar enthalpy of the phase  $\alpha$ .

The previous system of conservation equations is coupled to the following local closure laws:

$$\begin{cases} \sum_{\alpha \in Q} S^\alpha = 1, \\ \sum_{i \in \mathcal{C}^\alpha} C_i^\alpha = 1, & \alpha \in Q, \\ P^\alpha - P^\beta = P_c^{\alpha, \beta}(X), & \alpha \in Q, \quad \forall \beta \in Q, \alpha \neq \beta, \\ f_i^\alpha(P^\alpha, T, C^\alpha) = f_i^\beta(P^\beta, T, C^\beta), & \alpha \neq \beta, \quad (\alpha, \beta) \in (Q \cap \mathcal{P}_i)^2, \quad i \in \mathcal{C} \setminus \overline{\mathcal{C}_Q} \end{cases} \quad (3)$$

where  $P_c^{\alpha, \beta}(X)$  represents the capillary pressure between two distinct phases and the last equation describes the thermodynamic equilibrium for each component  $i$  present in at least two present phases,  $f_i^\alpha$  being the fugacity of component  $i$  in phase  $\alpha$ .

The system is finally closed by a flash calculation to determine the set of present phases (that is  $Q$ ) as a result of potential phase transitions:

$$Q = Q_{\text{flash}}(X). \quad (4)$$

136 **2.1.1 Hybrid model including discrete fractures and faults**

137 Special attention is paid in ComPASS to geological discontinuities such as faults or fracture  
138 networks, which can be drains and feedzones, also when they are crossed by the wells.

139 These discontinuities are thus taken into account explicitly in the model; they are represented  
140 by two dimensional embedded objects in the 3D rock mass. ComPASS uses the Discrete Fracture  
141 Matrix (DFM) approach with a lower dimension physical model associated with these objects, which  
142 is derived by averaging both the equations and the fault/fracture unknowns in their width.

143 The transmission conditions at the matrix fracture interfaces depend on additional physical as-  
144 sumptions concerning the fracture behavior, which may be drain or barrier. When faults or fractures  
145 are conductive both in terms of permeability and thermal conductivity, pressure and temperature  
146 continuity can be assumed as matrix fracture transmission conditions in single-phase flows [2, 12].  
147 This setting has been extended to two-phase Darcy flows in [11, 36, 13, 14] and to multi-phase  
148 compositional thermal Darcy flows in [42].

149 This approach explicitly accounts for discontinuities embedded in a discretized rock mass; it  
150 is particularly interesting in geothermal applications, where the flow may be dominated by the  
151 connectivity and conductivity of major discontinuities.

152 **2.1.2 Multi-branch well model**

153 One of the difficulty of well modeling in field simulation is the problem of the difference in scale  
154 between the reservoir size (several kilometers) and the wellbore radius (several centimeters). The well  
155 geometry cannot be resolved explicitly by the mesh; the well is then modeled as a line source defined  
156 by a 1D graph with a tree structure. This graph may effectively represent sloped and multi-branch  
157 wells; it is discretized by a subset of edges on which the mesh is based.

158 Flow in the well is locally coupled to the 3D matrix domain and to the faults/fractures crossing  
159 the well. The mass and heat exchanges for each node of the well in contact with a fracture or the rock  
160 mass are modeled with a Peaceman approach. It is a widely used approach in reservoir simulation  
161 for which the Darcy or Fourier fluxes between the reservoir and the well is discretized by a two-point  
162 flux approximation with a transmissivity accounting for the unresolved pressure or temperature well  
163 singularity. The well index or Peaceman's index [32] defined at the discrete level depends on the type  
164 of cell, on the well radius and geometry and on the scheme used for the discretization [41, 1, 15].

165 Regarding the flow model inside the well, it is assumed stationary. Using an explicit computation  
166 of the pressure drop, the well model is reduced to a single equation corresponding to the well moni-  
167 toring complementary conditions and a single implicit unknown corresponding to the well reference  
168 pressure (see e.g. [5]). The pressures and saturations along the well are then deduced from this  
169 reference pressure (and from the explicit in time expression of pressure losses).

170 The pressure drop model takes into account gravity pressure loss; moreover, a zero slip law is  
171 assumed in two-phase flow. These simplified well models could be easily extended to include non-  
172 zero slip laws as well as an explicit approximation of the wall friction along the wells. The well is  
173 monitored by prescribing complementary conditions between the mass flow rate and the wellhead  
174 pressure. For production (resp. injection) wells, they are based on a maximum (resp. minimum)  
175 mass flow rate and a minimum (resp. maximum) wellhead pressure.

176 Each well is thus associated with a single new unknown and equation. These new equations are  
177 added to the non-linear system. Note that by connecting all the nodes along the well trajectory  
178 to the well reference pressure unknown, the well equation introduces additional connectivity in the  
179 system to be solved, which must be considered when parallelizing the code.

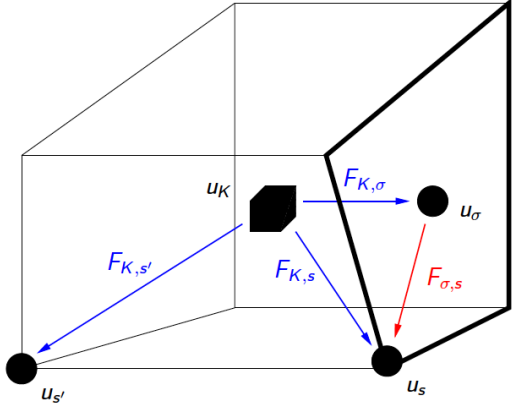


Figure 1: For a cell  $K$  and a fracture face  $\sigma$  (in bold), examples of VAG degrees of freedom  $u_K$ ,  $u_s$ ,  $u_{s'}$ ,  $u_\sigma$  and VAG fluxes  $F_{K,\sigma}$ ,  $F_{K,s}$ ,  $F_{K,s'}$ ,  $F_{\sigma,s}$ .

### 180 2.1.3 Discrete model

181  
182 The numerical scheme used by ComPASS is the Vertex Approximation Gradient (VAG) finite  
183 volume scheme [21], which belongs to the family of gradient schemes [19]. It is a scheme particularly  
184 adapted to the resolution of Darcy's law on polyhedral meshes. The VAG scheme deals with gener-  
185 alized polyhedral meshes of the simulation domain, which are assumed conforming: the cells may be  
186 star-shaped polyhedrons, and faces are not necessarily planar in the sense that they can be defined  
187 as the union of triangles joining the edges of the face to a so-called *face centre*.

188 The VAG discretization has been adapted to hybrid-dimensional (i.e. with 2D fractures and 1D  
189 wells in 3D rock-mass) modeling [12, 13]. This scheme has different degrees of freedom associated  
190 with: cells, cell nodes, fracture faces and wells (figure 1). The two main ingredients of this numerical  
191 scheme are the definition of fluxes between neighboring degrees of freedom and the assignment of a  
192 control volume to each of the unknowns.

193 Figure 1 shows one cell  $K$  with one fracture face  $\sigma$  in bold. The matrix fluxes (in blue on figure  
194 1) connect the cell  $K$  to the degrees of freedom located at the boundary of  $K$ : namely the cell nodes  
195 (e.g.  $F_{K,s}$  and  $F_{K,s'}$ ) and the fracture faces if any (e.g.  $F_{K,\sigma}$ ). The fracture fluxes (in red on figure  
196 1) connect each fracture face  $\sigma$  to its nodes (e.g.  $F_{\sigma,s}$ ). The expression of the matrix fluxes is linear  
197 and local to each cell as well as the expression of fracture fluxes is linear and local to each fracture  
198 face. Fluxes ensure the cell-cell, cell-fracture face and fracture face-fracture face connections.

199 Concerning the definition of control volume affected to each unknown, a choice of the cells and  
200 fracture faces partitioning defining the control volumes is done in order to avoid the mixture of  
201 heterogeneous properties inside each control volume: cell (resp. fracture face) volumes are split  
202 between the cell (resp. fracture face) centre and its boundary nodes (illustration on figure 2). For  
203 constant rocktypes per cell in the matrix and per face in the fracture network, the implementation  
204 of the scheme does not require to build explicitly the geometry of these partitions and it is sufficient  
205 to define the volume fractions.

206 The flexibility in the choice of the control volumes is a crucial asset, compared to other approaches  
207 such as Control Volume Finite Element Methods (CVFE). The VAG scheme has the advantage,  
208 compared to CVFE schemes, of avoiding the mixture of matrix and fracture media in the control  
209 volumes (see Figure 2), while keeping a cost of the same order as nodal methods on unstructured  
210 meshes [13]. Indeed, the VAG cell unknowns are eliminated without any fill-in from the Jacobian  
211 linear system during the numerical resolution.

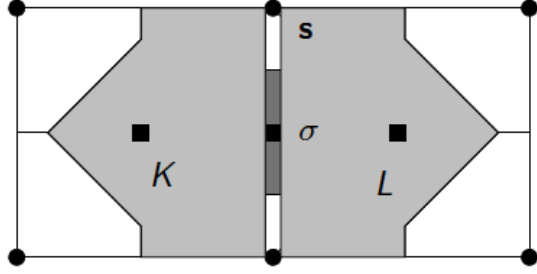


Figure 2: Example of control volumes at cells, fracture face, and nodes, in the case of two cells  $K$  and  $L$  split by one fracture face  $\sigma$  (the width of the fracture is enlarged in this figure). The control volumes are chosen to avoid mixing fracture and matrix rocktypes.

Two-phase Darcy flows discretization was introduced by Brenner *et al.* [13] and generalized to multi-phase multi-component flows by Xing *et al.* [42]. A phase based upwind scheme is used for the approximation of the mobilities in the Darcy fluxes. The time discretization is based on a fully implicit Euler scheme.

## 2.2 Numerical aspects

### 2.2.1 Non-linear solver

Spatial and temporal discretization of the system of conservation equations (eq. 2), including boundary conditions, results in a discrete non-linear system  $R_\nu(\mathbf{X}) = \mathbf{0}$  for each degree of freedom  $\nu$  with  $\mathbf{X} = (X_\nu)_{\nu \in \mathcal{D}}$  denoting the set of all unknowns (eq. 1) for all degrees of freedom  $\mathcal{D}$  (cells, cell nodes, fracture faces and wells). The problem is closed by adjoining a discrete non-linear version  $L_\nu(X_\nu) = 0$  of the closure laws and thermodynamic equilibrium (eq. 3).

Then the non-linear system to be solved at each time step writes in vector form  $\mathcal{R}(\mathbf{X}) = \mathbf{0}$  with:

$$\mathcal{R}(\mathbf{X}) = \begin{cases} R_s(\mathbf{X}) \text{ for each node } s, \\ L_s(X_s), \\ R_\sigma(\mathbf{X}) \text{ for each fracture centre } \sigma, \\ L_\sigma(X_\sigma), \\ R_K(\mathbf{X}) \text{ for each cell centre } K, \\ L_K(X_K), \\ R_w(\mathbf{X}) \text{ for each well } w. \end{cases} \quad (5)$$

The non-linear system  $\mathcal{R}(\mathbf{X}) = \mathbf{0}$  coupled to the flash fixed point equations (eq. 4) expressed locally at each degree of freedom is solved by an active set Newton-Raphson algorithm (e.g. Coats, [16]) which is detailed by Xing [42]. For each Newton-Raphson iteration the jacobian matrix is computed and a linear system is solved.

The set of unknowns is split into primary and secondary unknowns at each degree of freedom (except for the wells which only unknowns are the well reference pressures). The secondary unknowns are eliminated using the local closure laws. Moreover, for each Newton-Raphson iteration, the VAG cell unknowns are expressed as linear combinations of the nodes and fracture faces unknowns and eliminated too.

The resulting ill conditioned linear system is solved using an iterative solver (typically GMRES) combined with a preconditioner adapted to the elliptic or parabolic nature of the pressure unknown and to the coupling with the remaining hyperbolic or parabolic unknowns. One of the most efficient

236 preconditioners for such systems is the so-called CPR-AMG preconditioner [29, 38]. It combines mul-  
237 tiplicatively an algebraic multigrid preconditioner (AMG) for a pressure block (including the wellhead  
238 pressures) of the linear system with a more local preconditioner for the full system. Currently, the  
239 pressure equations defining the pressure block are obtained as the sum of the molar conservation  
240 equations in each control volume. Then an Incomplete LU factorization of order 0 is used for the  
241 full system (see [42]).

## 242 2.2.2 Meshing

243 Though meshing techniques are not the central part of our work, it is worth mentioning that ex-  
244 ploiting the full potentialities of the ComPASS code assumes to be able to produce quality conformal  
245 meshes out of complex geological models. A 3D mesh is described by dimensional spatial elements  
246 (vertices, edges, faces or cells) and set of adjacency relations between these elements that define the  
247 topology of the discretized model. A conformal mesh is a mesh such that intersection of any two  
248 distinct elements is either void either one, and only one, of the existing spatial elements. Moreover,  
249 there are several quality criteria concerning the mesh whose general idea is that the spatial elements  
250 are well proportioned not being too flat or distorted. Such ill proportioned elements are well known  
251 to create numerical difficulties in reservoir simulation. Though the VAG scheme performs noticeably  
252 well on such meshes [20], a good quality mesh will always make the simulation easier, especially when  
253 dealing with multi-phase simulations.

254 Though there has been a lot of progress in the recent years, producing a quality mesh out of  
255 complex geological models still remains an open problem in many aspects. A distinction is usually  
256 made between explicit and implicit geological models (*e.g.* [17]). On the one hand, the explicit  
257 modeling approach is based on a constructive methodology where the modeler edits and assembles  
258 sequentially geometric primitives. In simple cases, such as simple sedimentary basins, it can be rel-  
259 atively straightforward to generate 3D meshes by extruding the bi-dimensional mesh of a reference  
260 level along some directions (mesh pillars) producing prismatic (extrusion of triangles) or hexaedra  
261 (extrusion of quadrilaterals). The latter are referred as Corner-Point Grids in the oil industry or Ex-  
262 plicit Structured Grids, underlying the fact that they can be described using an underlying structured  
263 data. Such grids are typically non-conformable along discontinuities like faults. On the other hand,  
264 the implicit geological modeling approach is much more well suited to produce complex structural  
265 models with folded and faulted geological layers. In that case, most meshing techniques produce  
266 tetrahedral meshes and achieving fine control of the mesh characteristics is still a challenge. The  
267 fact that the VAG scheme is essentially nodal (using vertices as main degrees of freedom during the  
268 resolution step) makes it particularly suitable to work with this kind of meshes because tetrahedral  
269 meshes have much more cells than vertices.

270 In the subsequent examples we've been using the *Salome platform* to produce conformable  
271 meshes representing complex geological models. The approach is rather explicit in the sense that  
272 surfaces have been constructed first to represent either faults or layer boundaries. The surfaces  
273 composing such a B-Rep (Boundary Representation) model are then meshed with triangles. In a  
274 last step the meshing algorithm generates a tetrahedral discretization of the connected components  
275 between surface boundaries ([37, 39]). In the resulting mesh, structural surfaces (fractures/faults,  
276 layer boundaries) are discretized by triangulated surfaces while the well paths are defined by a  
277 connected sequence of edges. Each of these elements are tagged with specific codes using the Salome  
278 interface. The codes are then retrieved in the ComPASS simulation using a specific reader that can  
279 be used to assign different physical properties.

## 280 2.2.3 Application Programming Interface

281 Whereas previous versions of ComPASS, up to version 3, were implemented in pure Fortran

282 version 4 introduced a breaking change with the ability to set-up a simulation and control most of  
283 the timeloop execution using the high level Python language. The Python layer is not a mere set of  
284 routine to pre- or post process data but rather a full Application Programming Interface (API) with  
285 the long term ambition to provide a full numerical development environment for reservoir engineers  
286 and mathematicians.

287 As of today one of the main benefit of this API is to use the simplicity and efficiency of the Python  
288 language to set-up complex simulations or quickly adapt example scripts or explore simulation results.  
289 Some of the physical laws, such as relative permeabilities, capillary pressures, can also be specified  
290 by the user directly in Python without the need for compilation, either using an explicit formula  
291 or choosing one of the available models. The seasoned user can also build complex physical and/or  
292 numerical experiments (*e.g.* [3]) without the burden of recompiling the software and without loss  
293 of performance. As of today, output of the simulation are performed as compressed binary numpy  
294 arrays and post-processing routines are provided to convert them to *Paraview* parallel file formats.

#### 295 2.2.4 Parallel implementation

296 Both the assembly and resolution of linear systems involved in solving the fully coupled non-  
297 linear system (eq. 5) are done in parallel using the Single Program Multiple Data (SPMD) paradigm.  
298 For this purpose, the rows of the global system (eq. 5) are distributed in a well balanced manner to  
299 available processes. To be able to assemble these rows, degrees of freedom holding system unknowns  
300 (nodes  $s$ , fracture faces  $\sigma$ , cells  $K$  and wells  $w$ ) must also be distributed between processes, minimizing  
301 the need for communications.

302 At the beginning of the simulation, the set of cells of the mesh is first partitioned into subdomains  
303 using the METIS library [28]. Each of these subdomains is associated to a unique process rank. In  
304 the current implementation, this partitioning is only based on the cell connectivity graph and does  
305 not take into account the adjacency relations induced either by fractures or wells. In a second step,  
306 node and fracture degrees of freedom are distributed to processes according to the cells they are  
307 connected to. Elements belonging to the interior of a cell subdomain are unambiguously attributed to  
308 the associated process whereas an arbitrary but reproducible choice is made for boundary elements  
309 [42]. Ghost elements are then added to each subdomain to synchronize unknowns between adjacent  
310 degrees of freedom. One layer of ghost cells is added at the subdomain boundaries along with all the  
311 nodes and fractures elements that they intersect [42]. Concerning wells, well unknowns are associated  
312 to a mesh vertex (node) and are innately associated with the same process rank as this vertex.  
313 Nevertheless, all nodes belonging to a well path are created, and synchronized, in all subdomains  
314 intersecting the well path. By doing so, well state can be recomputed locally on any subdomain  
315 impacted by the well operations without communication between processes [8].

316 Once this distribution is made, meshes are reconstructed locally and at each Newton-Raphson  
317 iteration, a linear system that corresponds to rows of the system (eq. 5) is built locally on each  
318 process using both own and ghost (*i.e.* synchronized) unknowns. Once assembled, the system is  
319 transferred to the parallel linear solver library PETSc [6]. The way the parallel matrix and vector  
320 are stored in PETSc is in line with our choice as each process stores its own rows. The global linear  
321 system is then solved using the GMRES algorithm preconditioned by a CPR-AMG preconditioner  
322 as outlined previously. After resolution, the ghost unknowns are recovered by a synchronization step  
323 with MPI communications which is implemented using a PETSc matrix-vector product.

#### 324 2.2.5 Performance

325 We studied the performance and scalability of the code through various examples. As an il-  
326 lustration, we consider the case of a two-phase vertical well in a homogeneous reservoir (see [4] for  
327 details).

328     The geothermal reservoir is a parallelepipedic domain  $\Omega$  of size 2000 m  $\times$  2000 m  $\times$  200 m with  
 329     a vertical producer centered in the middle of the domain.

330     The reservoir is assumed to be homogeneous with isotropic permeability  $k_m = 5.10^{-14}$  m<sup>2</sup> and  
 331     porosity  $\phi_m = 0.15$ . The thermal conductivity is fixed to  $\lambda_m = 2\text{W.m}^{-1}\text{.K}^{-1}$  and the rock volumetric  
 332     heat capacity is given by  $c_r = 1.6\text{MJ.K}^{-1}\text{.m}^{-3}$ .

The simulation runs are performed for a family of refined uniform Cartesian meshes of size  $n_x \times n_y \times n_z$  of the domain with

$$(n_x, n_y, n_z) \in \{(10, 10, 5), (20, 20, 10), (40, 40, 20), (80, 80, 40)\}.$$

333     These meshes are labeled as  $\{h_1, \dots, h_4\}$  respectively. The well indexes are computed at each node  
 334     of the well.

335     A preliminary run is executed in order to have a stationary state in the reservoir [4]. Homogeneous  
 336     Neumann boundary conditions are prescribed at the bottom and at the top of the domain, and  
 337     Dirichlet boundary conditions for the pressure and temperature are fixed at the sides of the domain  
 338     to the ones obtained at the end of the preliminary run.

339     The well is open with a total flow rate of 200 t.h<sup>-1</sup> and a minimum well head pressure of 1 bar  
 340     (which is never reached in practice) during 30 days.

341     As detailed previously, at each time step the non-linear system is solved using a Newton-Raphson  
 342     algorithm. The GMRES stopping criterion on the relative residual is fixed to  $10^{-8}$ . The Newton  
 343     solver is convergent if the relative residual is lower than  $10^{-8}$  before a certain number of Newton  
 344     iterations. If the max number of iterations is reached, we consider that the time step has failed  
 345     (time step chop) and it is reduced. Table 1 shows the numerical efficiency of the proposed scheme  
 346     for all meshes during the production period. We denote by  $N_{\Delta t}$  the number of successful time  
 347     steps, by  $N_{\text{Chop}}$  the number of time step chops, by  $N_{\text{Newton}}$  the average number of Newton iterations  
 348     per successful time step, and by  $N_{\text{GMRES}}$  the average number of GMRES iterations per Newton  
 349     iteration. It exhibits a very good robustness of the Newton solver on the family of refined meshes  
 350     and a moderate increase of the number of GMRES iterations with the mesh size.

351     We present in Figure 3 the total computational time in hours obtained with the finest mesh  $h_4$   
 352     for different numbers of MPI processes  $N_p = 8, 16, 32, 64$ . As usual for this type of simulations,  
 353     the strong scalability is limited by the AMG preconditioner of the pressure block which requires  
 354     a sufficiently high number of unknowns per processor to keep a good scalability, corresponding to  
 355     roughly speaking  $5.10^4$ . This explains the very small speed-up between 32 and 64 processors whereas  
 356     the speed-up is good between 8 and 32 processors.

Mesh	# $\mathcal{M}$	$N_{\Delta t}$	$N_{\text{Chop}}$	$N_{\text{Newton}}$	$N_{\text{GMRES}}$
$h_1$	4000	134	0	1.99	8.59
$h_2$	32000	134	0	1.74	9.93
$h_3$	256000	134	0	1.92	11.75
$h_4$	1848320	133	0	2.22	15.91

Table 1: Numerical convergence behavior during the production period with respect to the mesh family.

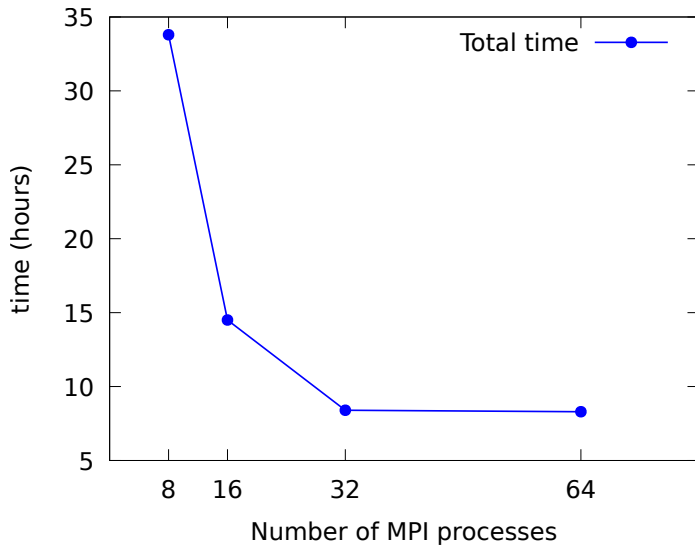


Figure 3: Total computational time vs. number of MPI processes for the production period simulation on the finest mesh  $h_4$ .

### 357 3 Numerical results and Case studies

358  
359     The software is developed using the Gitlab platform and uses continuous integration facilities to  
360     check new developments against several tests. The test database includes simple synthetic test cases  
361     and additional baseline test cases taken from geothermal code comparison projects [31]. Available  
362     tests may serve as tutorials and/or template for new simulations.

363     The next sections focus on large scale field studies and highlight the advantages of the ComPASS  
364     platform to describe complex geological settings and various physical conditions in geothermal explo-  
365     ration and production. The first three cases were built from reservoir studies and concern respectively  
366     an EGS-like fractured reservoir, a liquid dominated high enthalpy reservoir crossed by major faults  
367     and a high enthalpy low pressure steam reservoir. The last case is a two-component model describing  
368     the natural state of a geothermal system accounting for soil-atmosphere interaction and recharge.

#### 369 3.1 Deep geothermal liquid reservoir - EGS like

370     We study a geothermal reservoir located in a fractured basement at a depth of more than 4 km  
371     and a temperature of about 190°C. The modeled domain has an extension of 450 m  $\times$  900 m  $\times$  500 m  
372     and its top boundary is at a depth of 4 km. Fracturation is described by a discrete fracture network  
373     using three sets of fractures, referred as R, R2 and T and characterized by different orientations  
374     (Figure 4a).

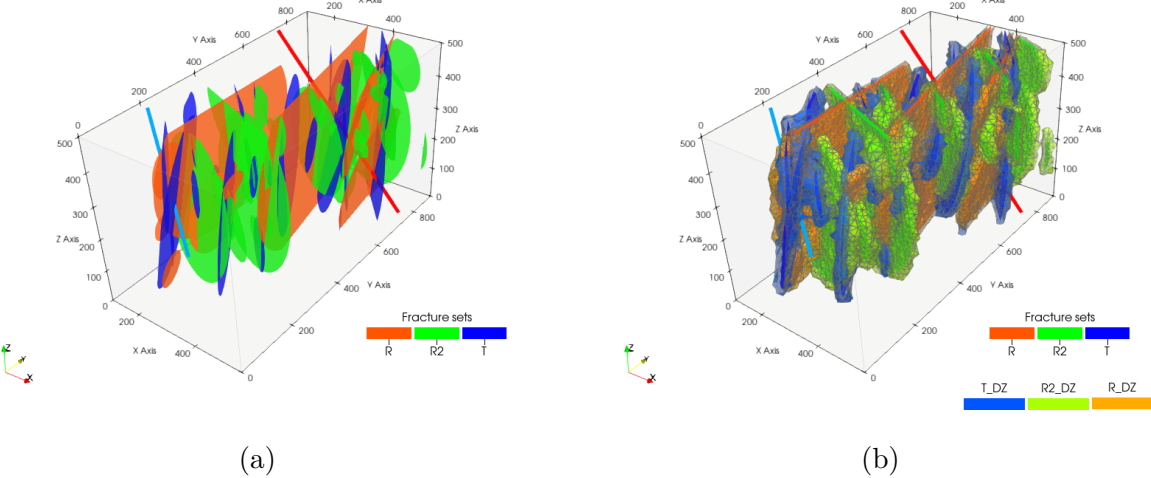


Figure 4: (a) Fracture sets embedded in the porous media and wells location - producer in blue and injector in red (b) Fracture sets and their associated damage zones and wells location.

The geothermal field is operated using a doublet of two deviated wells, a producer (in blue in Figure 4a) and an injector (in red in Figure 4a), both of which cross several fractures within the domain. The domain is meshed by a tetrahedral conformal mesh. This unstructured mesh is composed of more than 370000 tetrahedral elements; fracture surfaces and the two deviated wells are discretized by triangle facets and a set of edges belonging to some of tetrahedra, respectively.

The matrix (basement) surrounding the fracture sets is assumed to be homogeneous, weakly permeable with isotropic permeability of  $5.10^{-19} \text{ m}^2$  and a porosity of 0.15. Each fracture represents a higher permeable zone of 1 m thickness and 0.1 of porosity; R, R2 and T fracture sets have respectively a specific permeability of  $8.5 10^{-12} \text{ m}^2$ ,  $2.10^{-14} \text{ m}^2$  and  $1.10^{-13} \text{ m}^2$ . Each fracture is surrounded by an associated damage zone (Figure 4b), so-called here RDZ, R2DZ and TDZ with a specific permeability of  $8.5 10^{-13} \text{ m}^2$ ,  $2 10^{-15} \text{ m}^2$  and  $1.10^{-14} \text{ m}^2$ , respectively. The rock thermal properties are homogeneous for the whole rock mass with the thermal conductivity  $\lambda = 2.3 \text{ W.K}^{-1}.m^{-1}$ , the rock specific heat capacity is  $c_p = 800 \text{ J.kg}^{-1}.K^{-1}$ , and the rock density  $\rho_{rock} = 2650 \text{ kg.m}^{-3}$ .

The initial pressure state (Figure 5a) of the geothermal fractured system, is assumed hydrostatic (with approximately 370 bars at the top of the model). The temperature field (5b) increases linearly with depth (between 180°C at the top to 200°C at the bottom). No flow boundary conditions are applied on all faces of the domain and a heat flux of  $127 \text{ mW.m}^{-2}$  is imposed at the bottom boundary. Note that the fluid in the reservoir is in liquid state.

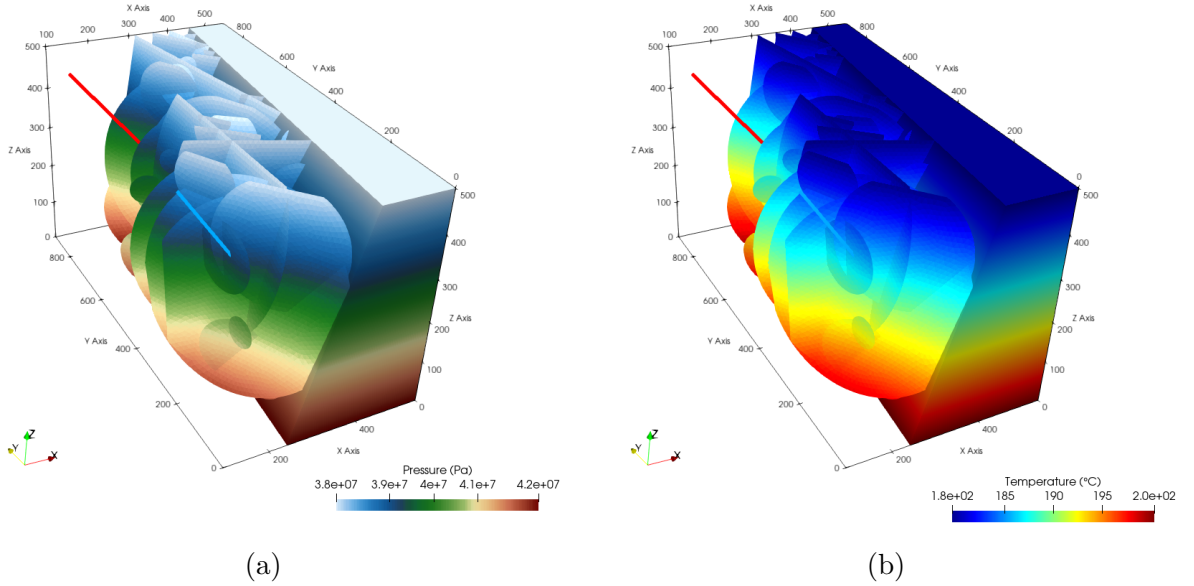


Figure 5: Initial pressure in Pa (a) and temperature in ( $^{\circ}\text{C}$ ) (b)

394     The reservoir is operated for fifty years with a constant flow rate of  $100 \text{ ton} \cdot \text{hr}^{-1}$  at the producer  
 395     well and a full reinjection of the produced fluid. The fluid is reinjected at a temperature of  $90^{\circ}\text{C}$ .  
 396     Figures 6 and 7 show the temperature evolution during the production. Fluid flow mainly occurs  
 397     within the fractures and to a lesser degree in damage zones.

398     At the beginning (first ten years), only fractures directly connected to the injector are impacted  
 399     by the cold fluid reinjection. The injected fluid migrates mainly along the R-fractures (which are  
 400     the most permeable), resulting in a rapid temperature decrease near these fractures, while cooling  
 401     in the matrix remains limited. After ten year of production, fractures that constitute the main fluid  
 402     flow path between the injector and the producer are already cooled and cold fluid starts to reach  
 403     the producer: the thermal breakthrough occurs (Figure 8a). In addition to the main fluid flow path  
 404     through the fractures, secondary flow paths occur through the damage zones (see Figure 7).

405     The produced fluid temperature decreases almost linearly with time after 15 years of exploitation  
 406     and reaches approximately  $142^{\circ}\text{C}$  after 50 years of production (Figure 8a). Enthalpy flow rate follows  
 407     the same behavior: it is constant during the first ten years (around  $2.2 \cdot 10^7 \text{ W}$ ) and then decreases  
 408     (Figure 8b).

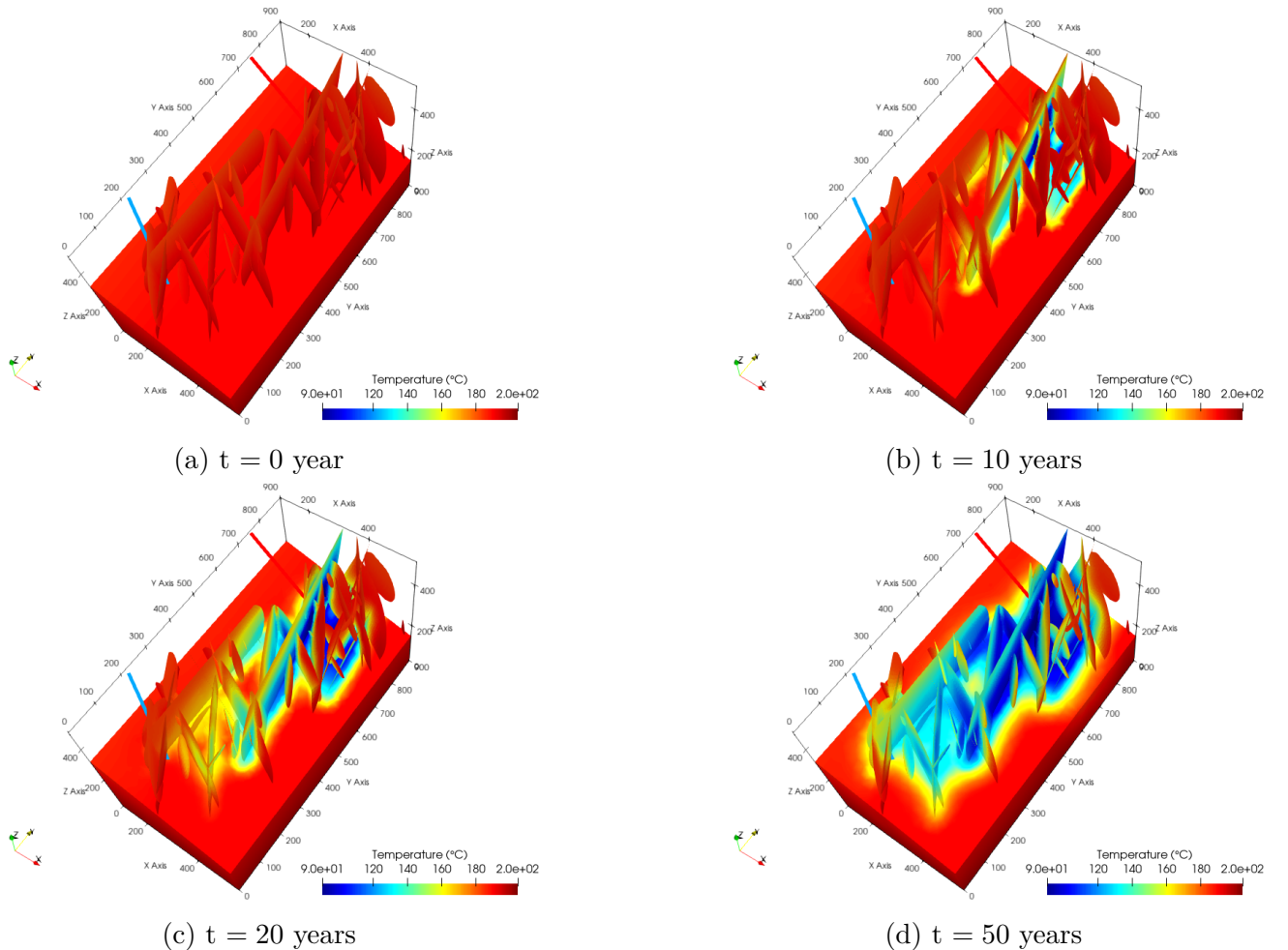


Figure 6: Temperature evolution ( $^{\circ}\text{C}$ ) within the faults and within the domain between 0 and 50 years.

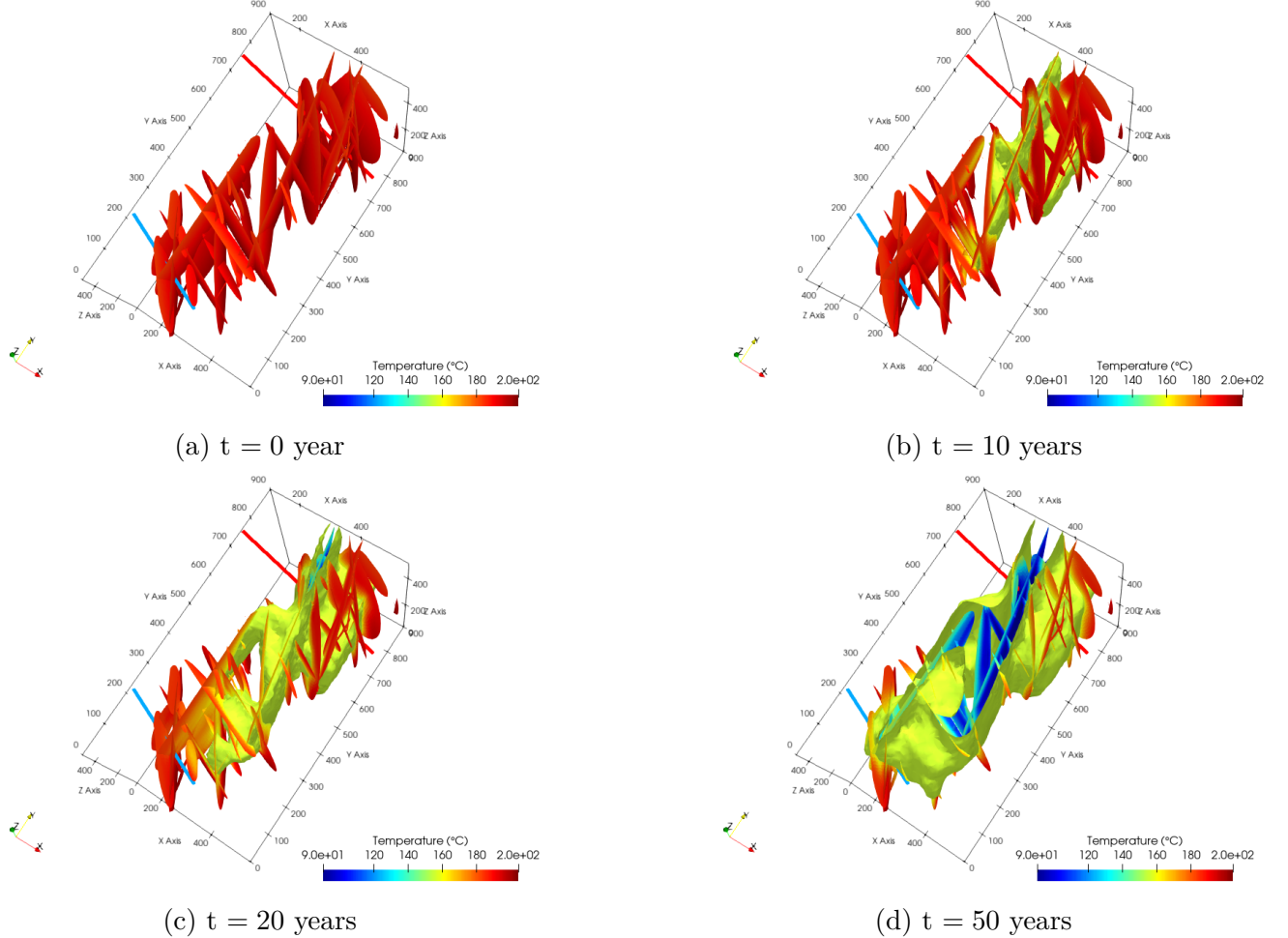


Figure 7: Temperature evolution ( $^{\circ}\text{C}$ ) within the faults and isosurface plot of the temperature  $155^{\circ}\text{C}$  between 0 and 50 years.

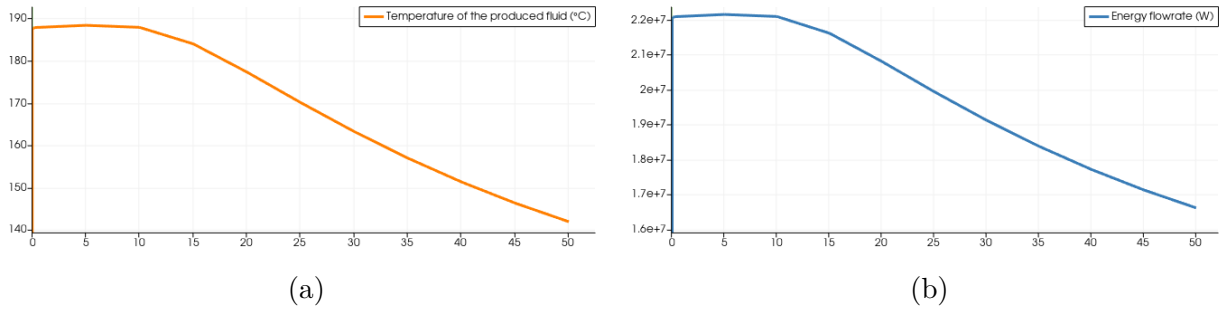


Figure 8: Temperature ( $^{\circ}\text{C}$ ) of the fluid (a) and energy flow rate (W) (b) at the producer well as function of time.

409 This test case demonstrates the flexibility of the ComPASS code, which makes possible to deal  
 410 with fracture network described explicitly.

### 411 3.2 Liquid dominated high enthalpy reservoir

412 In this section, we consider a case representative of a geothermal field in a volcanic area. The field  
 413 is a convection dominated system initially in liquid phase. A single component (water) two-phase

414 (gas, liquid) model is assumed.

415 The reservoir (blue domain in figure 9a) is about 500 m thick; it is covered by a weakly permeable  
 416 clay caprock (top yellow domain in figure 9a) of approximately 250 m thick, which outcrops at the  
 417 surface. Below the reservoir is the basement layer (bottom yellow domain in figure 9a). The reservoir  
 418 is crossed by several sub-vertical faults (figure 9a).

419 Figure 9b shows the tetrahedral mesh of the faulted domain. The mesh is conformal and made  
 420 of more than 100 000 nodes and composed of almost 600 000 tetrahedral elements. All surface  
 421 elements (geological horizons, fault surfaces) are discretized by triangle facets belonging to some of  
 422 the tetrahedra. Wells (one-dimensional elements) are discretized by a set of edges (Fig. 9b)

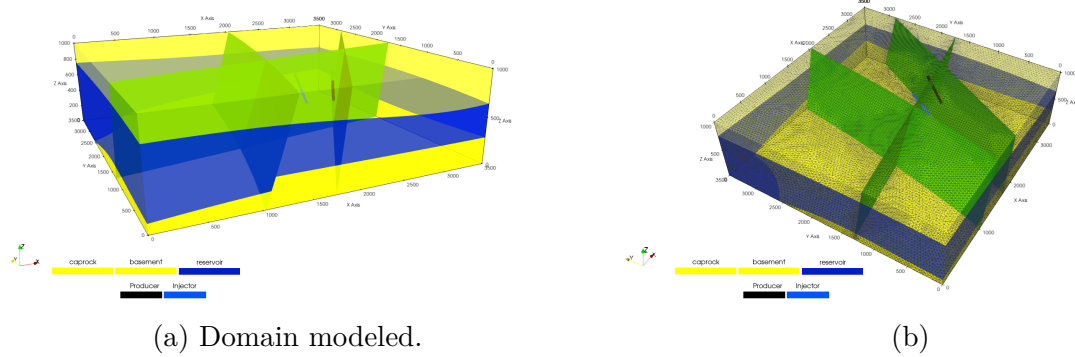


Figure 9: Geometry and mesh. (a) Domain modeled - (b) Mesh and wells location

423 The geothermal field is operated using a doublet of two deviated wells, a producer (black line in  
 424 Fig. 9b) and an injector (blue line in Fig. 9b), both of which cross one of the major faults within the  
 425 domain. The producer and the injector intersect the same fault at a depth of approximately 384m  
 426 and 405 m (below the surface), respectively.

427 The caprock and the basement layers have a low homogeneous and isotropic permeability of  $10^{-18}$   
 428  $\text{m}^2$ . The reservoir is assumed homogeneous with isotropic permeability of  $10^{-14} \text{ m}^2$  and a porosity of  
 429 0.05, while the faults are described by a damaged area of 10 m thickness, a permeability of  $5.10^{-14}$   
 430  $\text{m}^2$  and a porosity of 0.2. Note that the upper parts of the faults (in contact with caprock) are  
 431 considered low permeable. The rock thermal properties and density are homogeneous for the whole  
 432 rock mass with a thermal conductivity  $\lambda = 3 \text{ W.K}^{-1}.\text{m}^{-1}$ , a rock specific heat capacity  $c_p = 1000$   
 433  $\text{J}.\text{kg}^{-1}.\text{K}^{-1}$ , and a rock density  $\rho_{rock} = 2600 \text{ kg.m}^{-3}$ .

434 As a preliminary step, the initial state of the geothermal system, is achieved by performing a  
 435 simulation over a long period of  $10^5$  years from an hydrostatic pressure state (with 1 bar at the  
 436 top of the model) and a temperature field increasing linearly with depth (from 30°C at the top to  
 437 around 280°C at the bottom), until a stationary state is reached. Dirichlet boundary conditions  
 438 for temperature and pressure are imposed at the top and bottom boundaries. No flow boundary  
 439 conditions are considered on the four lateral boundaries. The initial state obtained after  $10^5$  years  
 440 is convective; temperature field is given in Figure 10. Iso-temperature surfaces of 190°C and 250°C  
 441 show the development of convection cells, influenced by the faults, which constitute highly permeable  
 442 drains. At the initial state, the fluid in the whole domain is in a liquid state (Fig. 11a). The producer  
 443 well (black line in Fig. 11a ) is located close to the intersection of two faults in order to exploit the  
 444 warmest (and shallowest) area, at the top of an upflowing plume, where the temperature is around  
 445 250°C.

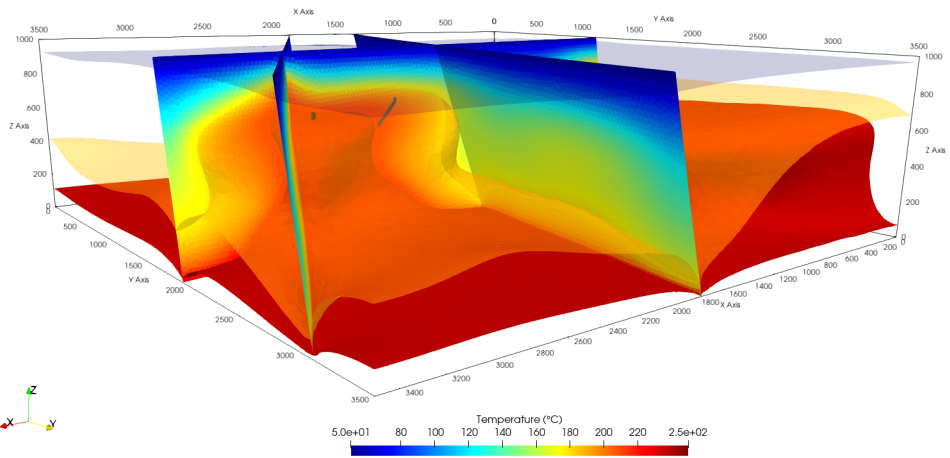


Figure 10: Isotemperature surfaces of 50°C, 190°C and 250°C at the initial state, dominated by convection.

The operating conditions simulation are as follows. Reservoir is produced with a constant flow rate of 180 ton. $\text{hr}^{-1}$  for three years without reinjection. After three years of production and depletion, injection starts: 80% of the fluid produced is reinjected at the injection well with a wellhead temperature of 110°C. Note that the same Dirichlet boundary conditions are imposed as for the initial state computation on the top and the bottom of the domain. Figure 11 shows the evolution of the temperature field close to the area of production (left) and the gas saturation (right) at multiple times. Note that during production, reservoir is not isolated and is partly recharged by faults.

In the early stages of production (i.e. before injection starts), the depletion near the producer well favors the development of a steam cap in the reservoir as well as in the fault zones (figure 11b). Steam accumulates at the top of the reservoir (where the gas saturation is equal to 1) below the low permeability caprock. As the fault is not completely sealed in the caprock, some migration of steam along the fault (Figure 11b) occurs. After three years, due to re-injection, the reservoir pressure increases, while steam around the injector condenses and the extension of steam cap generated around the producer is considerably reduced (Figures 11c and 11d). The re-injection impact on the steam cap is a very quick process as shown in the Figure 11c: the cloud of vapor has almost disappeared after 1 month. After 20 years of production, only a small fraction of steam may be observed in the reservoir close to the producer. Note that the upflowing plume delineated by the isotemperature surface of 250°C has been impacted by the cold fluid injection (its extension is clearly reduced in comparison with previous times, see Fig. 11d). The re-injection at a flow rate of 144 ton. $\text{hr}^{-1}$  (80% of the production) provides an efficient pressure support and then maintain conditions close to the natural state.

Figures 12 show the evolution of pressure (Figure 12a), temperature (Figure 12d), fluid enthalpy (Figure 12b) and gas saturation (Figure 12c) of the produced fluid in the producer well at a depth equal to that of the reservoir top and in the reservoir at the same depth over 10 years. The well is assumed open hole along its entire length in the reservoir.

In the early stages of production, pressures (in the well and in the reservoir at the top depth) decline rapidly (Figure 12a) and result in the production of steam in the well, the gas saturation in the well reaches its maximum value (around 0.9) after half a year (Figure 12c). Simultaneously the temperature of the produced fluid decreases from 245 °C to around 220°C (Figure 12d), due to the cooling effect of the vaporization. Note that in the meantime, the well enthalpy reaches around 1150 kJ/kg, which is higher than the initial fluid enthalpy (Figure 12b) in the reservoir. This excess enthalpy can be explained ([43]) by, on one hand, the higher mobility of steam compared to liquid

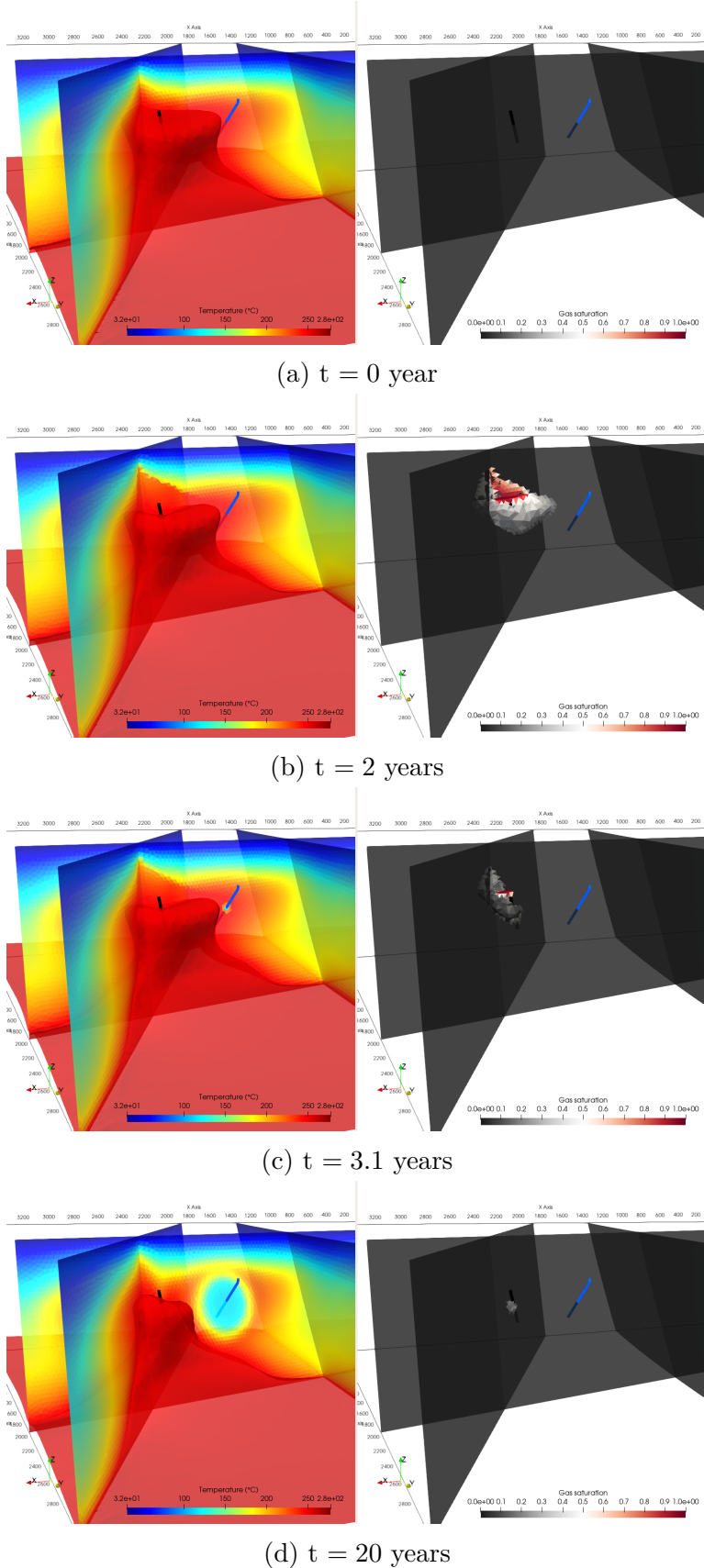


Figure 11: Left: Temperature evolution ( $^{\circ}\text{C}$ ) at multiple times within the faults and within the domain (isotemperature surface of  $250^{\circ}\text{C}$ ). Right: Gas saturation evolution (isosaturation surface of 0.1) at multiple times

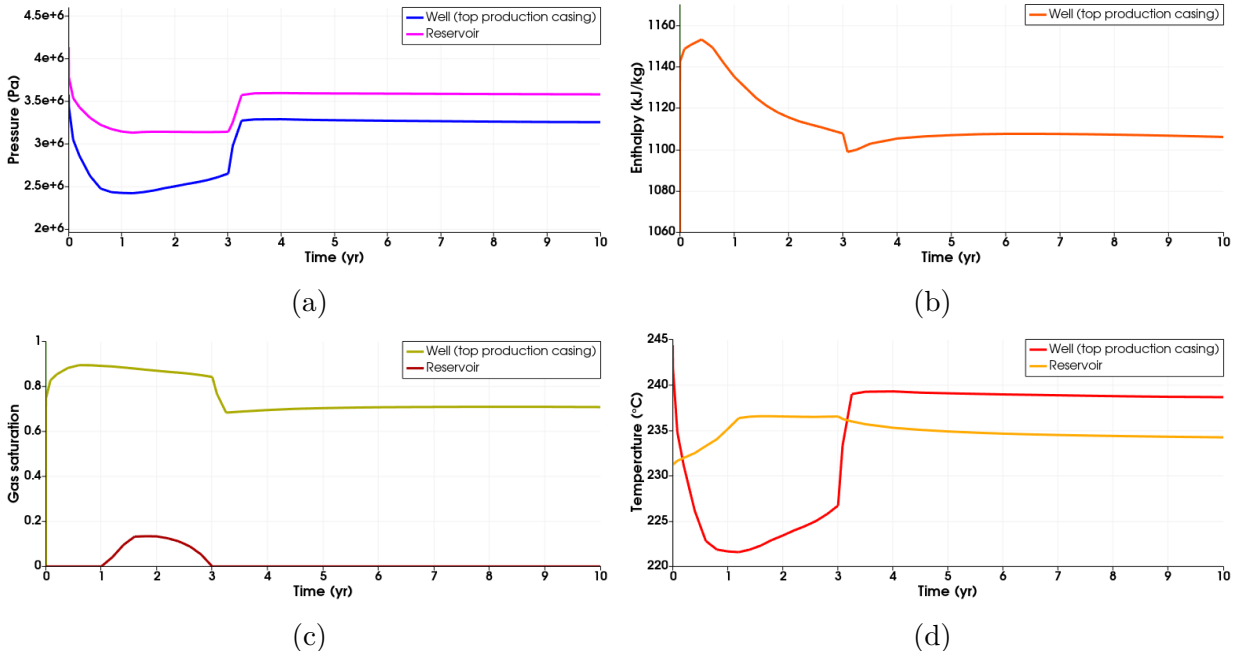


Figure 12: Main parameters at the top depth in the producer well and in the reservoir as function of time (a) Pressure - (b) Energy flow rate - (c) Gas saturation - (d) Temperature

479 water and on the other hand by an enhanced vaporization of the boiling water near the well ensured  
 480 by heat flow from the rock to the in place fluid. The excess enthalpy is transient. A decline of the  
 481 produced fluid enthalpy is then observed (Figure 12b) in conjunction with a slight decrease in gas  
 482 saturation (Figure 12c) in the well.

483 During this period, within the reservoir, the hot steam cloud migrates upward (temperature  
 484 increases at the top of the reservoir during the first year, see orange curve in Figure 12d), where  
 485 steam accumulates over time (Figure 11b). The accumulation (and expansion) of steam in the top  
 486 of the reservoir is characterized by a gas saturation that reaches its maximum saturation after two  
 487 years. This saturation then decreases due to the decline in boiling (dark red curve in Figure 12c),  
 488 while the reservoir temperature and pressure are maintained at constant values (Figures 12a and  
 489 12d).

490 The less intensive boiling results in a slight decrease in gas saturation, as well as a slight increase  
 491 in temperature and pressure in the well. From the third year, the injection starts, the producer is  
 492 quickly impacted due to pressure build-up (Figure 12a). The pressure build-up results in a rapid  
 493 decrease of gas saturation (around 15%, Figure 12c) as well as in an increase of the temperature of  
 494 the fluid produced in the well (Figure 12d) and a quick decline of the fluid enthalpy (Figure 12b).  
 495 Then, during the following years of exploitation, operating conditions remain relatively stable.

496 This test case illustrates the flexibility of ComPASS in order to model faults as objects in their  
 497 own right. In this example, two-phase flows occur both along and across faults, which strongly  
 498 influence the distribution of mass and energy flows in the reservoir during production.

### 499 3.3 Steam-dominated high enthalpy reservoir

500 This section is dedicated to the modeling of a low pressure high temperature steam-dominated  
 501 reservoir. The aim is to study the impact of the total reinjection of the produced fluid on the behavior  
 502 of a steam reservoir. A single component (water) two-phase (gas, liquid) model is assumed.

503 The domain studied is 2 km x 2 km x 4 km in size: a reservoir of 2 km thick is covered by a 2  
 504 km thick caprock (blue and yellow domains respectively in Figure 13). Note that the top limit of the

reservoir is modeled with a curved surface (concave shape). The geothermal field is operated using two deviated wells, a steam producer (in green) open only in the upper part of the reservoir and an injector (in blue) which crosses the whole reservoir (Figure 13).

The reservoir is assumed homogeneous in porosity and permeability, with an isotropic permeability of  $10^{-14} \text{ m}^2$  and a porosity of 0.035, while the thick overburden has low homogeneous permeability  $10^{-20} \text{ m}^2$  and porosity of 0.015. The rock thermal properties and densities are constant for the whole rock mass with a thermal conductivity  $\lambda = 2 \text{ W.K}^{-1}.\text{m}^{-1}$ , a rock specific heat capacity  $c_p = 1000 \text{ J.kg}^{-1}.\text{K}^{-1}$ , and a rock density  $\rho_{rock} = 2600 \text{ kg.m}^{-3}$ .

As a preliminary step, an initial state of the geothermal system is determined by performing a simulation over a long period (here  $10^4$  years) using the following initialization conditions: the caprock is assumed in liquid phase, a hydrostatic pressure state (with 1 bar at the top of the model) and a temperature field increasing linearly with depth (between 30°C at the top to 280°C at the bottom) are assumed, while the reservoir is two-phase with a gas saturation of  $S_g = 0.9$ , the initial pressure is equal to the saturation vapour pressure and the temperature field is assumed constant ( $T_{res} = 295^\circ\text{C}$ ). For the boundary conditions, Dirichlet boundary conditions for temperature and pressure are imposed at the top surface ( $T_{top} = 20^\circ\text{C}$  and  $P_{top} = 1\text{bar}$ ) and a high heat flux of 275  $\text{mW.m}^{-2}$  (Neumann boundary condition) is imposed at the bottom boundary. No flow boundary conditions are applied on the lateral boundaries.

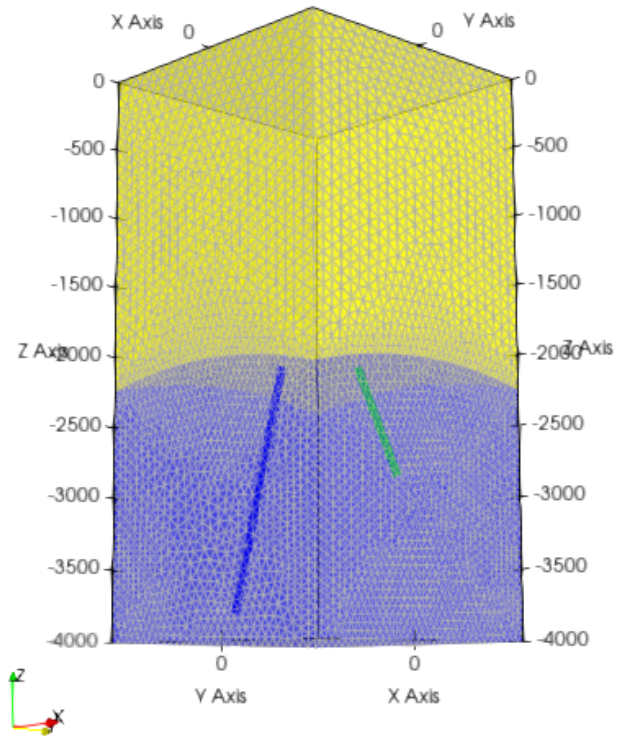


Figure 13: Domain modeled with the reservoir (in blue) and the caprock (in yellow), the mesh and the wells location : injector (in blue) and producer (in green).

At the initial state, a liquid zone remains at the bottom of the reservoir, while the remaining part of the reservoir is in gas phase; the caprock is in liquid state (Figure 14a). The pressure is hydrostatic in the caprock, while the initial pressure in the reservoir is around 80 bars (Figure 14b). The temperature increases linearly with depth within the caprock and is constant around 300°C in the reservoir, which is in a convective regime (Figure 14c and 15b).

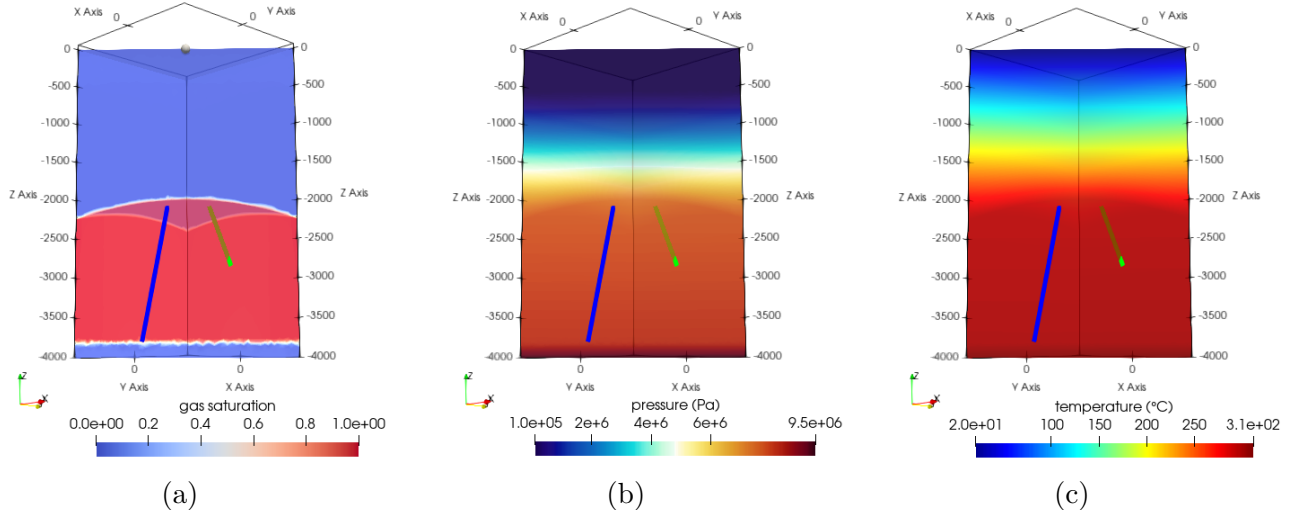


Figure 14: Initial state of the steam-dominated reservoir. (a) Gas saturation - (b) Pressure distribution (Pa) - (c) Temperature distribution (°C).

528     The reservoir is produced with a constant flow rate of  $75 \text{ ton.hr}^{-1}$ ; the condensed fluid is fully  
 529     reinjected with a temperature of  $110^\circ\text{C}$  at the wellhead. As in the previous case study, the same  
 530     boundary conditions are imposed as for the initial state computation.

531     Figures 16 show the distribution of pressure, gas saturation and temperature at the final state  
 532     after 30 years. A liquid cone has developed at the base of the injection well due to the cold reinjected  
 533     fluid, which favors steam condensation around the injector. Figures 15a and 15b show the vertical  
 534     pressure and temperature profiles, passing through the base of the injection well, at the initial and  
 535     final states. The steam pressure has decreased about 23 bars after 30 years of production, whereas  
 536     the gas-liquid interface has risen due to the reinjection of cold fluid.

537     In this test, ComPASS allows an accurate description of well locations (the mesh is based on  
 538     the location of wells) and condensation zones in two-phase modeling. This test case is based on a  
 539     reinjection study on a geothermal field in Italy.

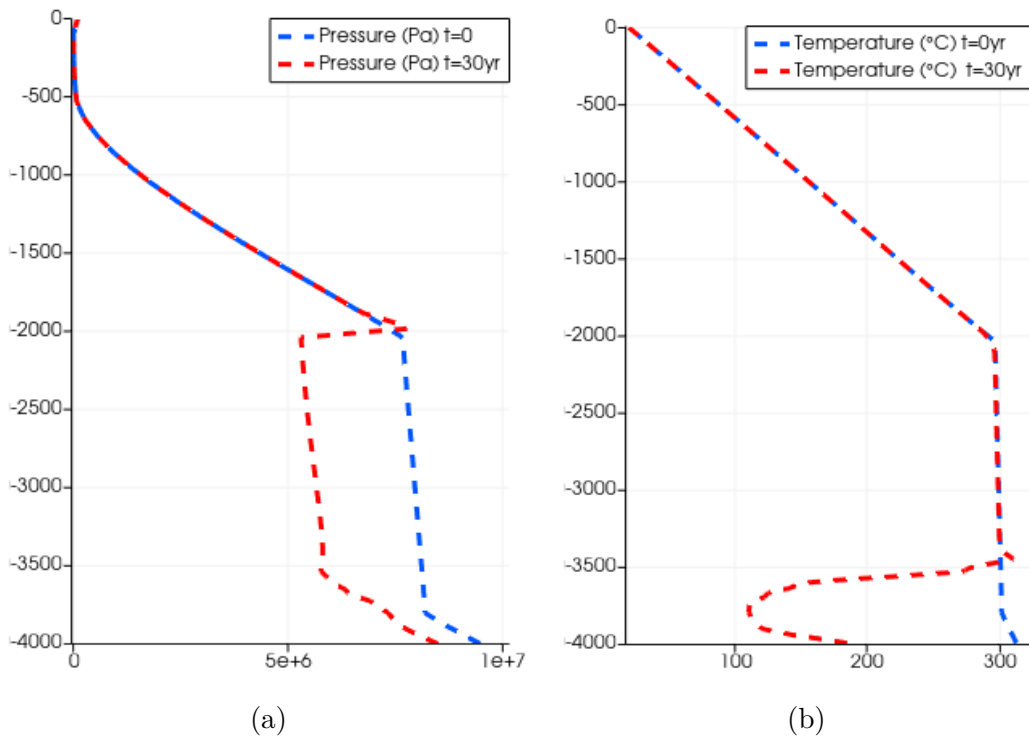


Figure 15: (a) Vertical pressure profiles (passing through the base of the injection well) - blue: initial pressure - red: after 30 years of production (b) Vertical temperature profiles (passing through the base of the injection well) - blue: initial temperature - red: after 30 years of production.

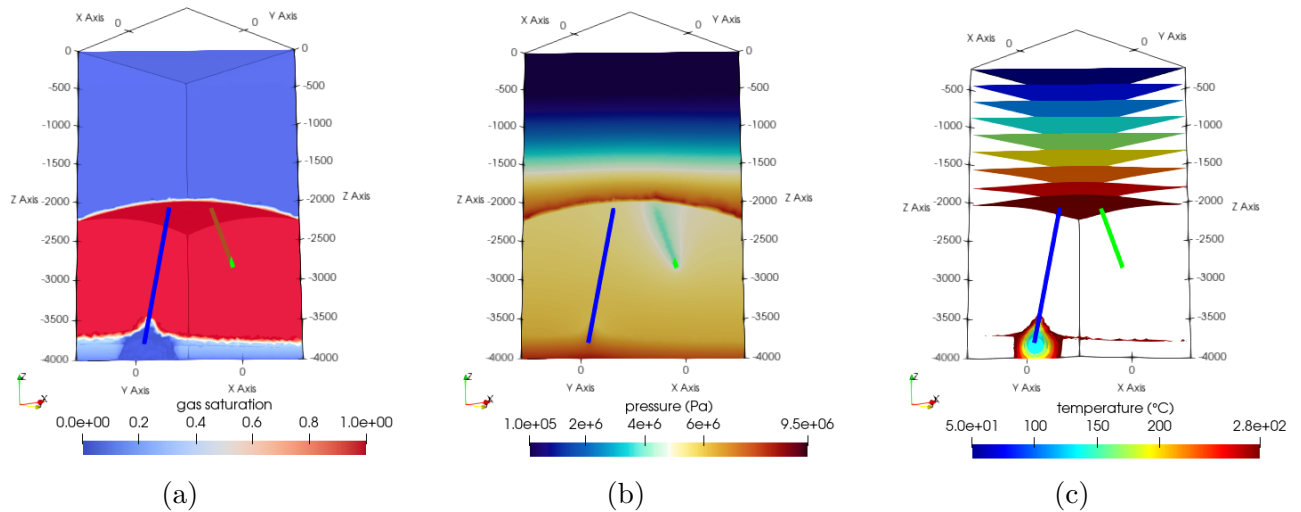


Figure 16: State of the reservoir after 30 years of production. (a) Gas saturation - (b) Pressure distribution (Pa) - (c) Temperature distribution ( $^{\circ}\text{C}$ ).

### 540 3.4 Volcanic island geothermal test case with soil-atmosphere interaction

542 This section is dedicated to the modeling of a faulted geothermal reservoir located in a volcanic  
 543 island context. The main aim of this model is to represent the natural state of a geothermal system.  
 544 The model describes the influence of the island topography on the flow pattern of hydrothermal

545 fluids in a volcanic complex. In particular, the distribution on the hot springs is modeled and thus  
 546 the impact of meteorological conditions on their temperature.

547 The ComPASS code simulates non-isothermal Darcy flows of gas-liquid composition (air and  
 548 water) taking into account soil-atmosphere exchanges [8]. The physics considered allows to model  
 549 the position of the water table and the vadose zone.

550 The domain studied is  $4 \times 4 \text{ km}^2$  and 2.5 km in depth. The elevation of the island reaches 300 m  
 551 above sea level (Figure 17). The island is surrounded by the sea and crossed by two main faults, the  
 552 two intersecting almost in the middle of the island.

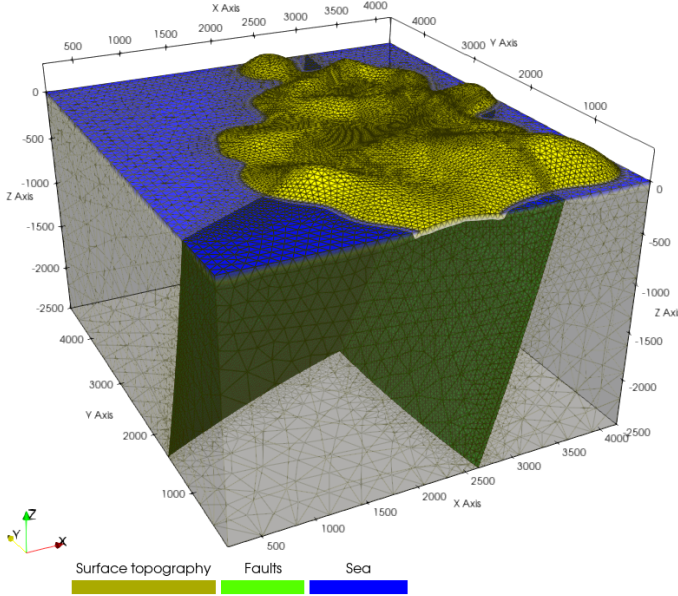


Figure 17: Domain modeled with the Island surface topography (in yellow), the sea (in blue), the faults (in green) and the mesh.

553 The domain is composed of three main parts: the emerged part of the island, the shallower part -  
 554 until 200 m below the sea level and the deeper part. Each part is assumed homogeneous in porosity  
 555 and permeability, with isotropic permeabilities of  $K_{m_{emerged}} = 10^{-13} \text{ m}^2$  and a porosity of 0.3 for the  
 556 emerged part,  $K_{m_{shallower}} = 10^{-14} \text{ m}^2$  and a porosity of 0.3 for the shallower part while the thick  
 557 deeper part has a lower homogeneous permeability  $K_c = 10^{-16} \text{ m}^2$  and porosity of 0.3. The rock  
 558 thermal properties and densities are constant for the whole rock mass with a thermal conductivity  
 559  $\lambda = 2 \text{ W.K}^{-1}.\text{m}^{-1}$ , a rock specific heat capacity  $c_p = 1000 \text{ J}.\text{kg}^{-1}.\text{K}^{-1}$ , and a rock density  $\rho_{rock} = 2600$   
 560  $\text{kg.m}^{-3}$ .

561 The initial state of the hydrothermal system is obtained by performing a preliminary simulation  
 562 step over a long period of time. The objective is to reach an equilibrium (average natural state) con-  
 563 sidering average atmospheric conditions (average annual temperature and precipitation). Constant  
 564 temperature, pressure and saturation are imposed ( $T_{top} = 13.3^\circ\text{C}$ ,  $P_{top} = 1\text{bar}$  and  $S_g = 0$ ) at the nodes  
 565 surrounding the island (sea), while the evaporation-outflow boundary condition [9] is imposed on the  
 566 topographic surface representing the emerged part of the island. The whole domain is considered  
 567 initially fully saturated with an hydrostatic pressure state (with 1 bar at the top) and a temperature  
 568 field increasing linearly with depth (from  $13.3^\circ\text{C}$  at the top to  $200^\circ\text{C}$  at the bottom). The atmospheric  
 569 conditions are set to  $C_a^{g,atm} = 0.8$  (air molar fraction in gas),  $C_w^{g,atm} = 0.2$  (water molar fraction in  
 570 gas),  $P_{atm} = 1 \text{ atm}$ ,  $T_{atm} = 13.3^\circ\text{C}$ ,  $q_w^{atm} = 0.021 \text{ mol.m}^{-2}.\text{s}^{-1}$ , where  $T_{atm}$  is the average annual  
 571 temperature and  $q_w^{atm}$  is an average water molar flow rate representing average annual precipitation

(estimated from the monthly temperature-rainfall chronicle Figure 18). These parameters are considered constant during the equilibrium step. Note that radiation absorbed and emitted by the soil surface are neglected in this model [8]. Finally a high heat flux of  $299 \text{ mW.m}^{-2}$  (Neumann boundary condition) is imposed at the bottom boundary of the fractures. No flow boundary conditions are applied on the lateral boundaries.

The initial state of the resulting geothermal system is given in Figure 19. Figure 19a shows the development of some surface water-saturated zones, which are located in the low elevation areas of the island. As shown by the Figure 19b these zones correspond to a preferential heat discharge area: they represent an hot spring. The existence of this spring results from the joint effect of advection produced across faults by the heat source at depth and subsurface flow at the near surface. The resulting hydraulic gradient significantly redistributes the heat flow. The temperature field along the faults (Figure 19) reflects these global water flows: cold water loops (up to 1 km depth) and highest temperature near the surface (preferential thermal discharge zone) are observed and are directly related to the recharge and discharge zones, respectively.

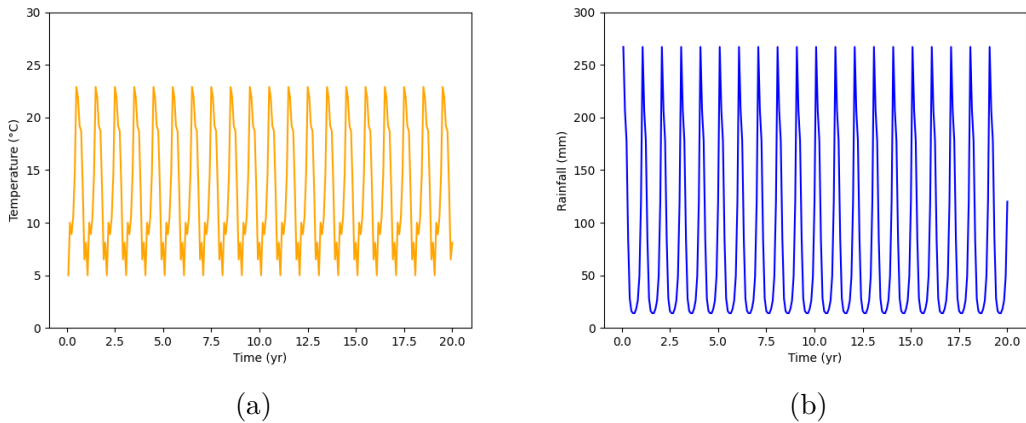


Figure 18: Monthly temperature-rainfall chronicle over a period of 20 years. (a) Monthly temperature chronicle ( $^{\circ}\text{C}$ ) (b) Monthly rainfall chronicle (mm).

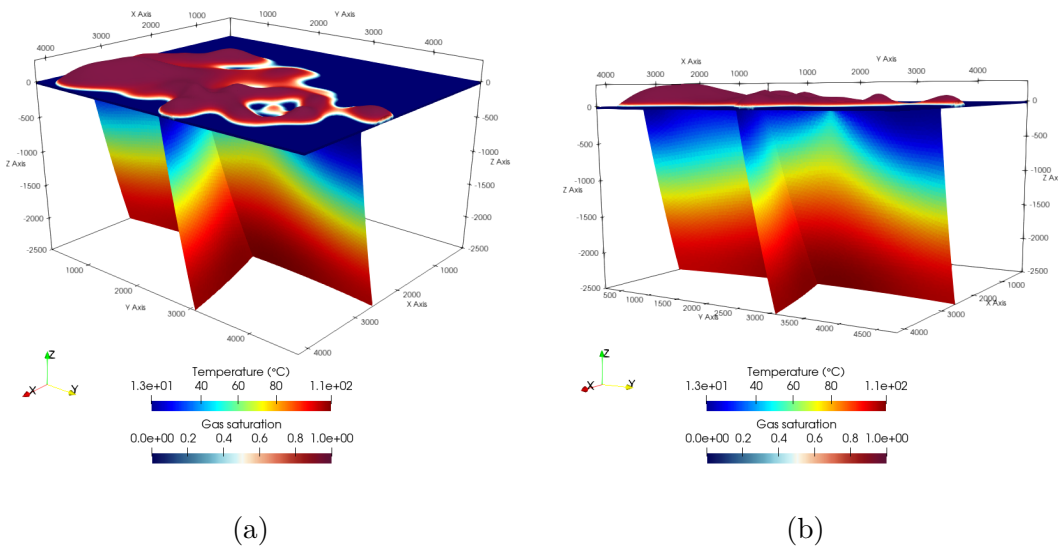


Figure 19: Initial states for gas saturation in the vadose zone (surface) and faults temperature (on fault planes) ( $^{\circ}\text{C}$ ). (a) Top view (b) Side view

586 A 20-year simulation is performed using the average monthly temperature-rainfall chronicle over  
 587 a year (replicated 20 times - Figure 18) in order to mimic the evolution of the hydrothermal system  
 588 under the influence of climate conditions.

589 The Figure 20 shows the hot spring temperature over time under the influence of meteorologi-  
 590 cal conditions (rainfall and temperature). Short temperature variations of the hot spring occurring  
 591 around the mean value of 40.2 °C are correlated to rainfall fluctuations where highest temperatures  
 592 correspond to rainy months (at the beginning and end of the year) and lowest temperatures cor-  
 593 respond to the drainer month. Indeed, more intense rainfall generates more intense water flowrate  
 594 from recharge area to discharge area, then the heat flux at the discharge area is higher and inversely.

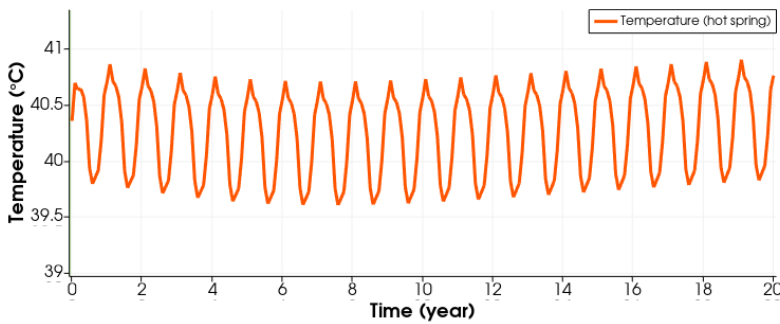


Figure 20: Fluid temperature (°C) at the hot spring as function of time

595 This test case shows how ComPASS can be applied to better understand the behavior of geother-  
 596 mal systems at large scale.

## 597 4 Conclusions

598 The modeling approach proposed in this paper is based on the use of unstructured meshes  
 599 in order to respect geometrical constraints. This choice of meshes adapted to complex geometries  
 600 requires in return to use an adapted numerical scheme, the VAG scheme, to model multi-phase and  
 601 compositional thermal physics (ComPASS solves multi-phase multi-component Darcy flows using a  
 602 Coats approach coupled with energy transfers). Moreover, particular attention is paid to faults and  
 603 fractures which are modeled as two-dimensional interfaces and to deviated wells which are reduced  
 604 to one-dimensional mesh objects. This approach is eased by the flexibility of the mesh used with the  
 605 VAG scheme.

606 The different test cases presented in this paper have shown that ComPASS can be used to perform  
 607 industrial studies in complex geological settings. The efficiency of the model in terms of ability to  
 608 account for complex geology in field applications is demonstrated on two-phase studies. Powerful  
 609 solver and the parallel implementation of the code ensure acceptable computation times on real case  
 610 studies.

611 The current developments concern on the one hand a multi-segmented well model accounting  
 612 for cross flows and on the other hand the implementation of equations of state and specific physics  
 613 for other applications such as the storage of nuclear waste or the underground storage of hydrogen.  
 614 For these applications, the use of an hybrid mesh combining polyhedral grid and structured regular  
 615 grid and numerical approach combining VAG and TPFA (Two point flux approximation) schemes is  
 616 under study.

## 617 Computer code availability

618 ComPASS is co-developed by BRGM and Université Côte d'Azur (LJAD - Inria). Core developers  
619 can be contacted through the mail alias compass.at.brgm.fr. The main evolutions of the core are  
620 implemented through projects. More information can be found at  
621 <https://charms.gitlabpages.inria.fr/ComPASS/index.html#credits>

622 The code is versioned using git and a repository is freely available at  
623 <https://github.com/loupantai/compass.git>. An online documentation is generated from the latest  
624 version and can be found at <https://charms.gitlabpages.inria.fr/ComPASS>. As of today the code  
625 runs under Linux OS (possibly through docker or WSL on Windows host system). The main re-  
626 quirements and dependencies can be found at  
627 <https://charms.gitlabpages.inria.fr/ComPASS/introduction.html#installation-instructions>. We pro-  
628 vide a conda environment which is designed to facilitate installation.

## 629 Acknowledgements

630 This work was funded by a partnership between BRGM and Storengy (rÃ©f. BRGM: RP21DGR054,  
631 STORENGY: EISE.DGSM.2021.00117).

632 The postdoctoral work of Daniel Castanon Quiroz was funded by BRGM and Storengy through  
633 a joint convention with Université Côte d'Azur (BRGM: 2019/104, STORENGY; STO1927RED,  
634 UCA/UNS: 2019/17).

635 The authors wish to acknowledge the use of CaSciModOT high performance computing facilities  
636 as part of this research (<https://cascimodot.fr/>).

## 637 References

- 638 [1] I. Aavatsmark and R. Klausen. Well Index in Reservoir Simulation for Slanted and Slightly  
639 Curved Wells in 3D Grids. *SPE Journal*, 8(01):41–48, 03 2003.
- 640 [2] C. Alboin, J. Jaffré, J. Roberts, and C. Serres. Modeling fractures as interfaces for flow and  
641 transport in porous media. volume 295, pages 13–24, 2002.
- 642 [3] L. Amir and M. Kern. Jacobian Free Methods for Coupling Transport with Chemistry in  
643 Heterogenous Porous Media. *Water*, 13(3), 2021.
- 644 [4] A. Armandine Les Landes, D. Castanon Quiroz, L. Jeannin, S. Lopez, and R. Masson. Two-phase  
645 geothermal model with fracture network and multi-branch wells. *submitted*, 2022.
- 646 [5] Z. P. Aunzo, G. Bjornsson, and G. S. Bodvarsson. Wellbore Models GWELL, GWNACL, and  
647 HOLÄ, user's guide. Technical Report LBL-31428, Earth Sciences Division, Lawrence Berkeley  
648 National Laboratory, University of California, 1991.
- 649 [6] S. Balay, M. Adams, J. Brown, P. Brune, K. Buschelman, V. Eijkhout, and H. Zhang. PETSc  
650 Users Manual. Revision 3.5. Technical report, 2015.
- 651 [7] L. Beaude. *Numerical simulation of non-isothermal compositional two-phase flows in porous*  
652 *media and its applications to high energy geothermy*. Phd thesis, Université Côte d'Azur, Dec.  
653 2018.

- 654 [8] L. Beaude, T. Beltzung, K. Brenner, S. Lopez, R. Masson, F. Smai, J.-f. Thebault, and F. Xing.  
 655 Parallel Geothermal Numerical Model with Fractures and Multi-Branch Wells. *ESAIM: Pro-*  
 656 *ceedings and Surveys*, 63:109–134, Oct. 2018.
- 657 [9] L. Beaude, T. Beltzung, K. Brenner, S. Lopez, R. Masson, F. Smai, J.-f. Thebault, and F. Xing.  
 658 Parallel geothermal numerical model with fractures and multi-branch wells. *ESAIM: ProcS*,  
 659 63:109–134, 2018.
- 660 [10] L. Beaude, K. Brenner, S. Lopez, R. Masson, and F. Smaï. Non-isothermal compositional liquid  
 661 gas Darcy flow: formulation, soil-atmosphere boundary condition and application to high-energy  
 662 geothermal simulations. 23, 2019.
- 663 [11] I. I. Bogdanov, V. V. Mourzenko, J.-F. Thovert, and P. M. Adler. Two-phase flow through  
 664 fractured porous media. *Physical Review E*, 68(2), aug 2003.
- 665 [12] K. Brenner, M. Groza, C. Guichard, G. Lebeau, and R. Masson. Gradient discretization of  
 666 hybrid-dimensional Darcy flows in fractured porous media. *Numerische Mathematik*, 134(3):569–  
 667 609, nov 2016.
- 668 [13] K. Brenner, M. Groza, C. Guichard, and R. Masson. Vertex Approximate Gradient scheme for  
 669 hybrid-dimensional two-phase Darcy flows in fractured porous media. *ESAIM: Mathematical  
 670 Modelling and Numerical Analysis*, 2(49):303–330, 2015.
- 671 [14] K. Brenner, M. Groza, L. Jeannin, R. Masson, and J. Pellerin. Immiscible two-phase Darcy flow  
 672 model accounting for vanishing and discontinuous capillary pressures: application to the flow in  
 673 fractured porous media. *Computational Geosciences*, 21(5):1075–1094, Dec 2017.
- 674 [15] Z. Chen and Y. Zhang. Well flow models for various numerical methods. *J. Numer. Anal.  
 675 Model.*, 6:375–388, 2009.
- 676 [16] K. Coats. Implicit compositional simulation of single-porosity and dual-porosity reservoirs. In  
 677 *SPE Symposium on Reservoir Simulation*. Society of Petroleum Engineers, apr 1989.
- 678 [17] P. Collon and G. Caumon. 3D Geomodelling in Structurally Complex Areas - Implicit vs.  
 679 Explicit representations. In *EAGE Conference & Exhibition 2017*, pages 1–4, June 2017. Issue:  
 680 June 2017.
- 681 [18] A. Daniilidis, S. Saeid, and N. G. Doonechaly. The fault plane as the main fluid pathway:  
 682 Geothermal field development options under subsurface and operational uncertainty. *Renewable  
 683 Energy*, 171:927–946, 2021.
- 684 [19] J. Droniou, R. Eymard, T. Gallouët, and R. Herbin. A unified approach to mimetic finite  
 685 difference, hybrid finite volume and mixed finite volume methods. *Math. Models Methods Appl.  
 686 Sci.*, 20(2):265–295, 2010.
- 687 [20] R. Eymard, C. Guichard, and R. Herbin. Benchmark 3D: the VAG scheme. In J. Fořt, J. Fürst,  
 688 J. Halama, R. Herbin, and F. Hubert, editors, *Finite Volumes for Complex Applications VI  
 689 Problems & Perspectives*, pages 1013–1022, Berlin, Heidelberg, 2011. Springer Berlin Heidelberg.
- 690 [21] R. Eymard, C. Guichard, and R. Herbin. Small-stencil 3D schemes for diffusive flows in porous  
 691 media. *ESAIM: Mathematical Modelling and Numerical Analysis*, 46(2):265–290, 2012.
- 692 [22] R. Eymard, C. Guichard, R. Herbin, and R. Masson. Vertex-centred discretization of multiphase  
 693 compositional Darcy flows on general meshes. *Computational Geosciences*, 16(4):987–1005, 2012.

- 694 [23] M. A. Grant and P. F. Bixley. Preface to the second edition. In M. A. Grant and P. F. Bixley,  
 695 editors, *Geothermal Reservoir Engineering (Second Edition)*, pages xv–xvi. Academic Press,  
 696 Boston, second edition edition, 2011.
- 697 [24] S. Hirschberg, S. and Wiemer and P. Burgherr. Energy from the Earth : Deep Geothermal as a  
 698 Resource for the Future ? Technical report, 2015.
- 699 [25] Y. Huang, Y. Cheng, L. Ren, F. Tian, S. Pan, K. Wang, J. Wang, Y. Dong, and Y. Kong.  
 700 Assessing the geothermal resource potential of an active oil field by integrating a 3d geological  
 701 model with the hydro-thermal coupled simulation. *Frontiers in Earth Science*, 9, 2022.
- 702 [26] S. Jalilinasrably, T. Tanaka, R. Itoi, and H. Goto. Numerical simulation and production  
 703 prediction assessment of takigami geothermal reservoir. *Energy*, 236:121503, 2021.
- 704 [27] M. Karimi-Fard, L. Durlofsky, and K. Aziz. An efficient discrete-fracture model applicable for  
 705 general-purpose reservoir simulators. *SPE Journal*, 9(02):227–236, jun 2004.
- 706 [28] G. Karypis and V. Kumar. A Fast and high quality multilevel scheme for partitioning irregular  
 707 graphs. *SIAM Journal on Scientific Computing*, 20(1):359–392, jan 1998.
- 708 [29] S. Lacroix, Y. V. Vassilevski, and M. F. Wheeler. Decoupling preconditioners in the implicit  
 709 parallel accurate reservoir simulator (IPARS). *Numerical Linear Algebra with Applications*,  
 710 8(8):537–549, dec 2001.
- 711 [30] F. Magri, T. Akar, U. Gemici, and A. Pekdeger. Deep geothermal groundwater flow in the  
 712 seferihisar-balçova area, turkey: results from transient numerical simulations of coupled fluid  
 713 flow and heat transport processes. *Geofluids*, 10(3):388–405, 2010.
- 714 [31] M. W. Molloy and M. L. Sorey. Code Comparison Project – A Contribution to Confidence in  
 715 Geothermal Reservoir Simulators. *Geothermal Resources Council Transactions*, 1981.
- 716 [32] D. Peaceman. Interpretation of Well-Block Pressures in Numerical. *Reservoir Simulation Sym-  
 717 posium Journal SEPJ*, pages 183–194, 1978.
- 718 [33] D. Peaceman. Interpretation of Well-Block Pressures in Numerical Reservoir Simulation with  
 719 Nonsquare Grid Blocks and Anisotropic Permeability. *Reservoir Simulation Symposium Journal  
 720 SEPJ*, pages 531–543, 1983.
- 721 [34] M. Person, A. Hofstra, D. Sweetkind, W. Stone, D. Cohen, C. W. Gable, and A. Banerjee.  
 722 Analytical and numerical models of hydrothermal fluid flow at fault intersections. *Geofluids*,  
 723 12(4):312–326, 2012.
- 724 [35] M. Raguenel, T. Driesner, and F. Bonneau. Numerical modeling of the geothermal hydrology  
 725 of the volcanic island of basse-terre, guadeloupe. *Geothermal Energy*, 7(28), 2019.
- 726 [36] V. Reichenberger, H. Jakobs, P. Bastian, and R. Helmig. A mixed-dimensional finite volume  
 727 method for two-phase flow in fractured porous media. *Advances in Water Resources*, 29(7):1020–  
 728 1036, jul 2006.
- 729 [37] A. Ribes and C. Caremoli. Salomé platform component model for numerical simulation. In  
 730 *31st Annual International Computer Software and Applications Conference (COMPSAC 2007)*,  
 731 volume 2, pages 553–564, 2007.

- 732 [38] R. Scheichl, R. Masson, and J. Wendebourg. Decoupling and block preconditioning for sedi-  
733       mentary basin simulations. *Computational Geosciences*, 7(4):295–318, 2003.
- 734 [39] J. Schöberl. Netgen an advancing front 2d/3d-mesh generator based on abstract rules. *Com-*  
735       *puting and Visualization in Science*, 1:41–52, 1997.
- 736 [40] M. A. Simms and G. Garven. Thermal convection in faulted extensional sedimentary basins:  
737       theoretical results from finite-element modeling. *Geofluids*, 4(2):109–130, 2004.
- 738 [41] C. Wolfsteiner, L. J. Durlofsky, and K. Aziz. Calculation of well index for nonconventional wells  
739       on arbitrary grids. *Computational Geosciences*, 7(1):61–82, 2003.
- 740 [42] F. Xing, R. Masson, and S. Lopez. Parallel numerical modeling of hybrid-dimensional composi-  
741       tional non-isothermal darcy flows in fractured porous media. *Journal of Computational Physics*,  
742       345:637–664, sep 2017.
- 743 [43] S. J. Zarrouk and K. McLean. Chapter 2 - geothermal systems. In S. J. Zarrouk and K. McLean,  
744       editors, *Geothermal Well Test Analysis*, pages 13–38. Academic Press, 2019.